

1
2 **Spectroscopic detection of terrestrial lightning from space by JUICE-MAJIS**
3 **during Earth Gravity Assist**
4

5 Emiliano D'Aversa⁽¹⁾, Fabrizio Oliva⁽¹⁾, Giuseppe Piccioni⁽¹⁾, François Poulet⁽²⁾, Ivana
6 Kolmašová⁽³⁾, Benoît Seignovert⁽⁴⁾, Alessandra Migliorini⁽⁵⁾, Gianrico Filacchione⁽¹⁾, Leigh
7 Fletcher⁽⁶⁾, Alessandro Mura⁽¹⁾, Yves Langevin⁽²⁾, Davide Grassi⁽¹⁾, Sébastien Rodriguez⁽⁷⁾,
8 Federico Tosi⁽¹⁾, Nicolas Ligier⁽²⁾, Giuseppe Sindoni⁽⁸⁾, Marco Giardino⁽⁸⁾, Christina Plainaki⁽¹⁾
9

10 (1) Istituto Nazionale di Astrofisica, INAF-IAPS, Via del Fosso del Cavaliere 100, 00133, Rome,
11 Italy.

12 (2) Institut d'Astrophysique Spatiale, CNRS/Université Paris-Saclay, 91405 Orsay Cedex,
13 France.

14 (3) Department of Space Physics, Institute of Atmospheric Physics of the Czech Academy of
15 Sciences, Prague, Czechia.

16 (4) OSUNA, UAR-3281, LPG UMR-6112, CNRS, Nantes Université, Nantes, France.

17 (5) Istituto Nazionale di Astrofisica, INAF-OAPd, 35122 Padova, Italy.

18 (6) School of Physics and Astronomy, University of Leicester, University Road, Leicester, LE1
19 7RH, UK.

20 (7) Université Paris Cité, Institut de physique du globe de Paris (IPGP), CNRS, Paris, France.

21 (8) Italian Space Agency, Via del Politecnico snc, 00133, Rome, Italy.
22
23

24 _____
25
26 Correspondence to: emiliano.daversa@inaf.it
27
28
29
30
31
32
33
34
35
36
37
38
39
40
41
42
43
44
45
46
47

48
49
50
51
52
53
54
55
56
57
58
59
60
61
62
63
64
65
66
67
68
69
70
71
72
73
74
75
76
77
78
79
80
81
82
83
84
85
86
87
88
89
90
91
92
93
94
95

Abstract

A lightning event was detected by the MAJIS imaging spectrometer onboard the Jupiter Icy Moons Explorer (JUICE) spacecraft during its first Earth gravity assist maneuver. This serendipitous observation represents the first space-based spectroscopic measurement of lightning for any planetary atmosphere. The event, composed of four flashes, was registered on 2024, August, 20th in an area offshore of Sumatra island, during local nighttime, near to optically thick clouds probed by MAJIS thermal wavelengths. No coincident detection has been obtained by ground-based lightning sensor networks, yet MAJIS observations provide unambiguous evidence of neutral atomic oxygen and nitrogen emissions, identified through several diagnostic lines. A faint H α signature may also tentatively be associated with lightning flashes.

As MAJIS is not optimized for such observations, a number of caveats related to spectral and temporal resolutions have been considered when deriving absolute quantities, such as lightning energy and temperature. Retrieved energies are overall consistent with known emission by lightning of average strength, ranging from (0.7 ± 0.2) to (1.3 ± 0.3) MJ in the 777 nm O I line and from (0.5 ± 0.2) to (1.5 ± 0.4) MJ in the 870 nm N I line. Estimates of the temperature of the lightning channel yield a broad range of values, spanning between 5000 and 20000 K, with standard uncertainties of the order of 2000-3000 K depending on the retrieval method. This is ascribed to a higher sensitivity to biases induced by the limited measurement resolutions.

Overall, this observation represents a useful benchmark for guiding detection and interpreting possible lightning events on Jupiter, a primary target of the JUICE mission. A preliminary extrapolation of the terrestrial case to the conditions of Jovian atmosphere suggests that H I emissions in the 650 nm and 1870 nm spectral ranges are the most promising for identifying lightning on Jupiter with the MAJIS instrument.

96
97
98
99
100
101
102
103
104
105
106
107
108
109
110
111
112
113
114
115
116
117
118
119
120
121
122
123
124
125
126
127
128
129
130
131
132
133
134
135
136
137
138
139
140
141
142

1. Introduction

In its journey to the Jovian system, the JUICE spacecraft performed a close flyby at Earth (Earth Gravity Assist, EGA) on 2024, Aug, 20, about one day after a similar close encounter with the Moon (Lunar Gravity Assist, LGA). Despite the very low flyby altitude (6100 km at minimum), and the consequent high velocity profile, the maneuver allowed the scientific instruments onboard to acquire several datasets, mainly aimed at testing their performances as well as those of the ground-segment. During EGA, the onboard Moon And Jupiter Imaging Spectrometer (MAJIS) collected 19 scans (data cubes) covering the spectral range 500-5560 nm. An extensive overview of the full sequence from both technical and scientific point of views can be found in Poulet et al. (this issue).

In the present work we only focus on the first cube of the EGA sequence, where unexpected emissions were found at visible wavelengths on Earth's nightside. These signals suggest a serendipitous detection of lightning flashes originated in a thunderstorm cloud, whose location and thickness are appreciable in simultaneous thermal imaging.

In the following Sect.2 we describe in detail the observations and the adopted methods of analysis. Although the observations are not optimal for physical studies of lightning, we attempt to derive the energies and temperatures involved, by applying specific corrections, assessing a useful framework for investigating possible other similar observations by imaging spectrometers. Main results are mostly presented in Sect.3 and discussed in Sect.4. An overview of lightning spectroscopy on Earth and other planets is presented at the beginning of Sect.4. To our knowledge, MAJIS lightning observations presented in this work constitute the first case of an unambiguous direct spectroscopic observation of lightning from space, on any planet. Conclusions are summarized in Sect.5.

2. MAJIS observations

2.1. Data description and processing

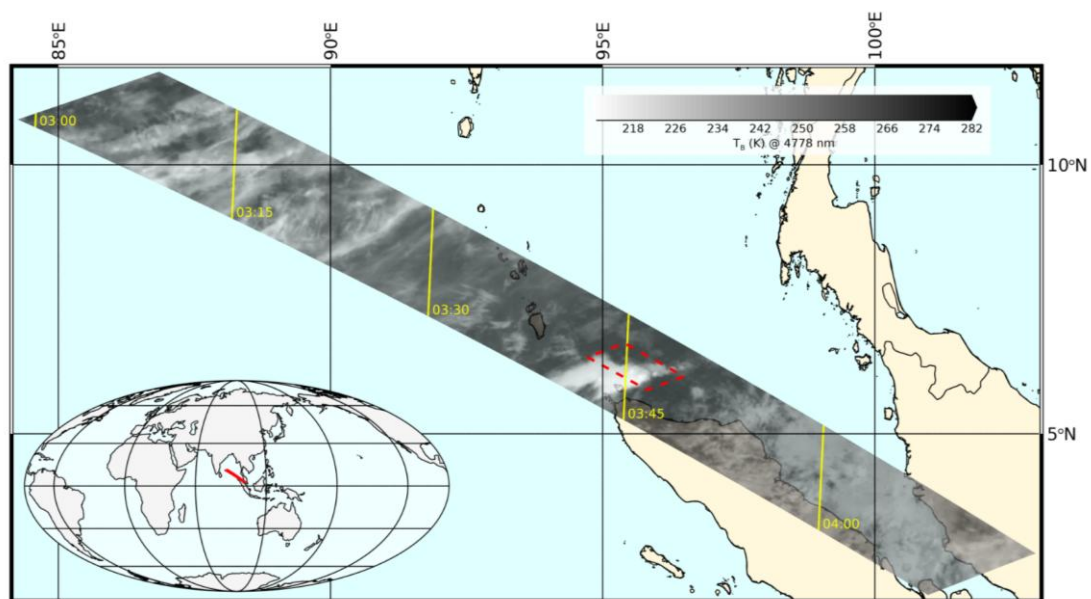
The Moon And Jupiter Imaging Spectrometer (MAJIS) is an imaging spectrometer covering the spectral range 500-5560 nm in two separate channels (VISNIR and IR), with a boundary at a wavelength around 2300 nm. Spectral bands' characteristics are variable depending on instrument setting, with nominal VISNIR Full Widths at Half Maximum (FWHMs) of the order of 3.5-5.6 nm and sampling of 3.6-3.7 nm/band, and slightly larger values for IR channel (FWHM 6.6-8.5 nm and sampling 6-7 nm/band) (Haffoud et al., 2024). Both channels work with 2-dimensional detectors that, sharing the same field of view, can acquire a variety of spectral scans of a target in a push-broom acquisition scheme. The direction of the field of view during a scan is controlled by either changing the whole spacecraft pointing or by rotating an internal mirror, or both. Descriptions of the instrument, its operations and calibration are detailed in Poulet et al. (2024a), Filacchione et al. (2024), Haffoud et al. (2024), Langevin et al. (2024), Rodriguez et al. (2024), Vincendon et al. (2024), and Stefani et al.(2025). Observing geometry reconstruction is based on NAIF-SPICE libraries and tools (Acton, 1996; Acton et al., 2018) and kernels provided by ESASPACE Service (JUICE Operational SPICE Kernel Dataset, 2019).

143 While we refer the reader to Poulet et al. (this issue) for a detailed overview of the MAJIS
144 EGA observations, here we only focus on the first data cube of the sequence (UTC start time
145 2024-08-20T21:25:09), where unexpected emissions are seen in the VISNIR channel. No other
146 similar emissions have been found in other data cubes of the same sequence.

147 The cube under investigation covers an area offshore northern Sumatra island, across
148 the Andaman Sea (Figure 1). It is fully registered at nighttime (local time~03:30) hence the
149 presence of clouds can only be appreciated at thermal wavelengths, simultaneously covered by
150 MAJIS IR channel (shown in terms of brightness temperature in the figure). Although the
151 footprint extends over some land areas, no evident variations of thermal emission appear in
152 association with coastlines, suggesting overall cloudy conditions thick enough to prevent land
153 detection.

154 The scan is composed of 128 samples (pixels along slit direction), 865 frames (pixels
155 across slit direction) and 1016 bands (spectral dimension, equally distributed between VISNIR
156 and IR channels), with nominal spatial and spectral binning implemented. It has been obtained
157 by rotating the line of sight by about 4° (2° of rotation of the internal mirror) in 865 steps for a
158 total time of 173 seconds. At every step (i.e. every 200 ms), a 128-pixels spectral frame
159 encompassing 1016 wavelengths has been acquired, with an integration time of 22 ms. The
160 mirror movement caused the ground footprint to move at about 9.4 km/s, spanning almost 10°
161 in latitude (from 11.7°N to 2.0°N). At the same time, the spacecraft was moving rapidly eastward,
162 with a ground projected velocity component of about 6.6 km/s. Since no spacecraft active
163 pointing could be implemented, the resulting MAJIS boresight motion at the ground was at about
164 ~11.5 km/s in the southeast direction, explaining the slant footprint projection shown in Figure
165 1.

166 The area where lightning is detected is near the middle of the MAJIS scan (red box in
167 Figure 1), acquired when the spacecraft was flying at about 11500 km above the surface. In this
168 condition, the MAJIS instantaneous field of view (150 μrad) is projected to a spatial resolution
169 of about 1.7 km/pixel. However, the motion smearing accumulated during the 22 ms integration
170 yields a slight enlargement of the pixel area (f) by an amount ~10% (and an average linear
171 resolution degrading to ~2 km/pixel).

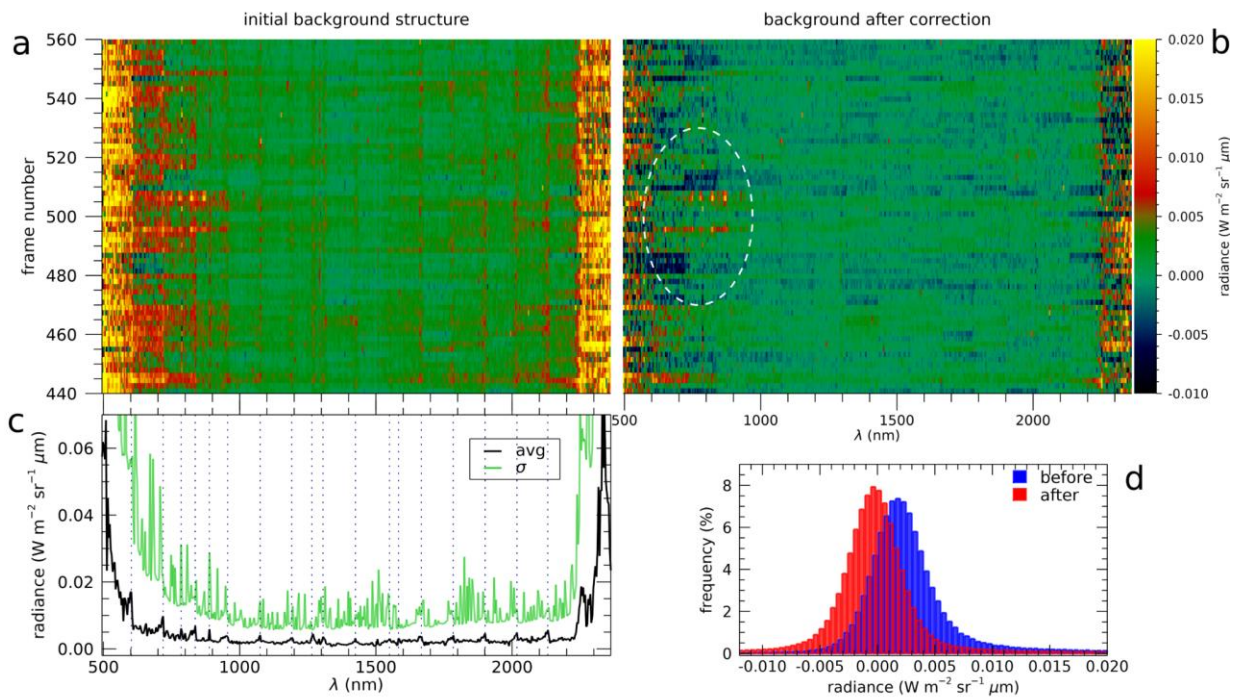


172
173 **Figure 1-** Projection of the first MAJIS scan of the EGA sequence, where visible lightning
174 emissions are detected. The covered area extends over the Andaman Sea and partially over
175 Sumatra island, and Nicobar Archipelago. The gray-scale map represents the brightness

176 temperature as registered by MAJIS at 4611 nm wavelength. The red box indicates the area
 177 of potential lightning detection, detailed in Figure 2. Coastlines are obtained from
 178 OpenStreetMap and are available under Open Database License.

179
 180 As the data were acquired at nighttime, the signal registered at VISNIR wavelengths
 181 outside the lightning area is instrumental noise. The search for potential signatures of known
 182 diffuse sources of emission from the Earth atmosphere, like airglows (e.g. the auroral-triggered
 183 O I green line at 557.7 nm, Levenko et al., 2019) yields no significant results. This fact simplifies
 184 the study of the background fluctuations statistics which is very helpful for deriving absolute
 185 intensities and suitable detection thresholds (Noise Equivalent Spectral Radiance, NESR) for
 186 lightning emissions. As we can see in Figure 2, the background noise is enhanced at both
 187 spectral edges of the VISNIR channel. The subtraction from the data cube of the average
 188 spectral background is effective in reducing this issue, narrowing the overall background
 189 distribution and allowing lightning signals to emerge more clearly as a statistical anomaly (Figure
 190 2). This analysis yields an average detection limit (NESR) for this observation, after background
 191 correction, of $2 \cdot 10^{-3} \text{ W/m}^2/\text{sr}/\mu\text{m}$. It is worth stressing that a significant residual background
 192 pattern is still present after correction at the edges of the VISNIR channel, even if limited to the
 193 ranges below 700 nm and above 2200 nm.

194



195
 196 **Figure 2** - Data preprocessing for background correction. The VISNIR background for a cube
 197 subset encompassing lightning signatures (frames 400-600 and averaged over the samples
 198 60-70) are shown in the upper panels, before (Panel a) and after (Panel b) background
 199 correction. Lightning emissions are located near frame 500, highlighted by the dashed ellipse
 200 in the upper right panel. Panel c shows the spectrum of the average background before
 201 correction (black curve), which is used for the cube correction, with its associated standard
 202 deviation (green curve), not affected by background removal. Finally, Panel d shows the
 203 comparison of the whole cube background distribution before/after the correction.

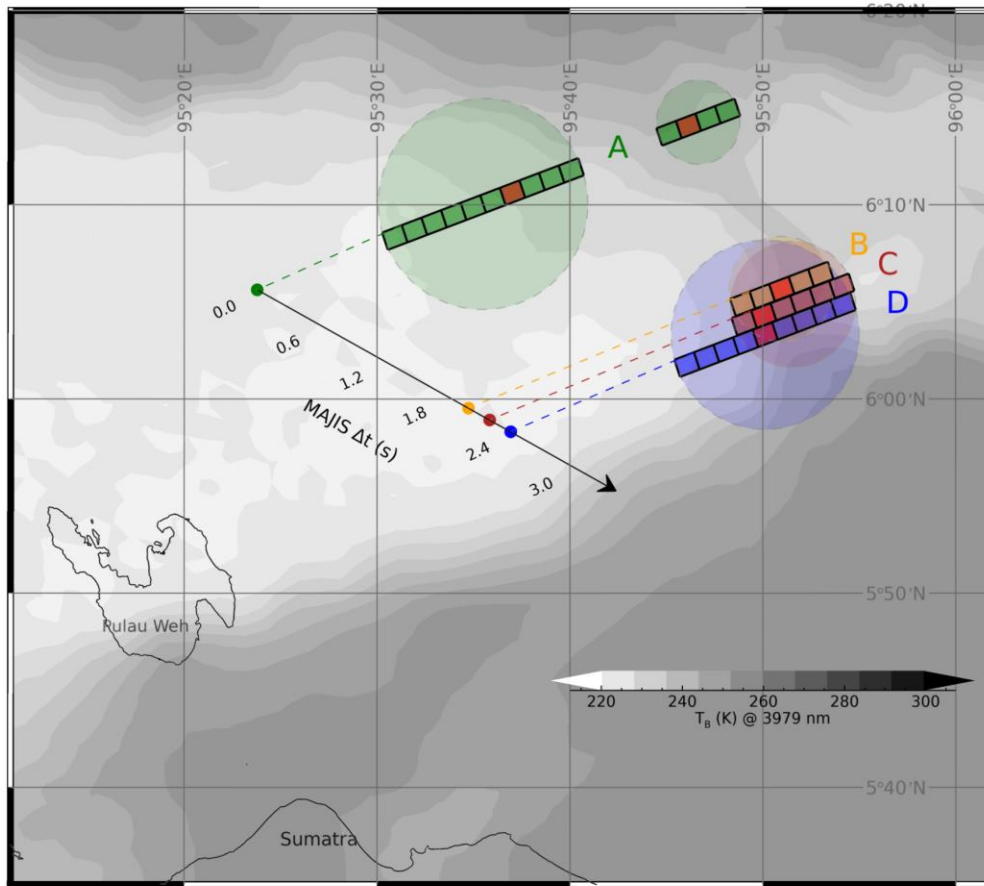
204
 205

206
207
208
209
210
211
212
213
214
215
216
217
218
219
220
221
222
223
224
225
226
227
228
229

2.2. Lightning location and spatial considerations

The exact locations of lightning signatures are identified by using the radiance thresholds derived from background analysis (see previous Sect.2.1). Figure 3 shows the footprints of those pixels where a signal exceeding 3-times the NESR has been found in more than one spectral band. They are shown projected on the Earth surface against the same thermal image displayed in Figure 1. The pushbroom acquisition scheme implies that, while the instrument boresight moves (in the arrow direction in Figure 3), all pixels along the same spectral frame (A, B, C, D labels in Figure 3) are simultaneously acquired. Therefore, these aligned pixels can actually represent a portion of a larger flash area, whose extension could be guessed from the total length of the illuminated portion of the slit. Assuming a circular shape, the corresponding flash areas extrapolated from the involved MAJIS frames are shown color-shaded in Figure 3. Basic properties of these flashes are given in Table 1. The significant overlapping in the case of B, C and D frames in Figure 3 opens the possibility that MAJIS observed a unique lightning flash sequence there.

It is worth stressing that this kind of observation cannot resolve the light directly emitted by the lightning channel, which is a few centimeters thick, but is rather sensitive to the light scattered by the surrounding clouds, known to spread for several kilometers from the source. Global statistics report average sizes of scattered lightning flash of about 25 km (e.g. Rudlosky et al., 2019, give mean areas of 454 km² over land and 570 km² over ocean), close to the lengths measured in MAJIS flash observations (Table 1), which can therefore be considered as spatially resolved.



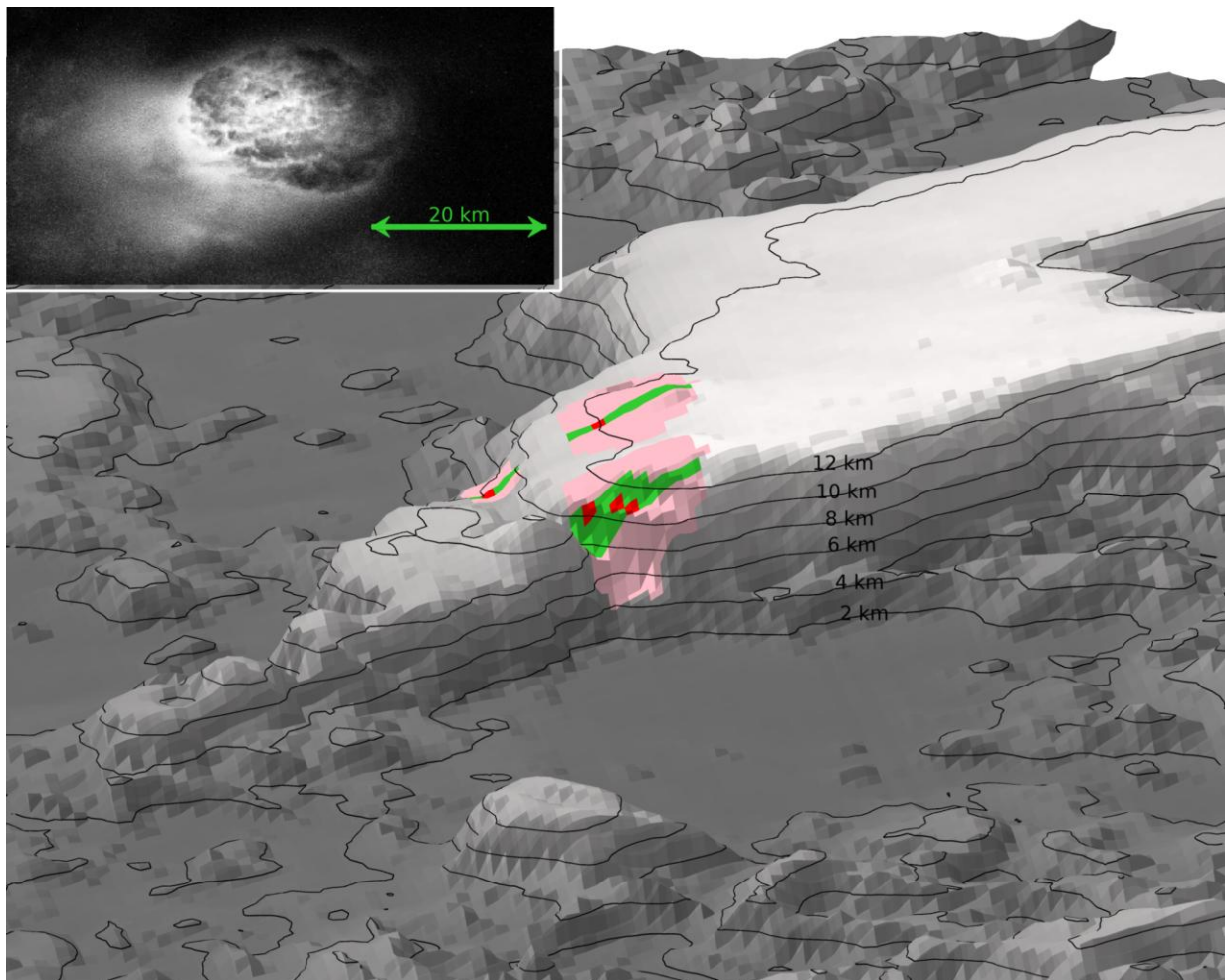
230
 231 **Figure 3-** The footprints of MAJIS lightning pixels are indicated by the colored squares, shown
 232 against a brightness temperature map (same of Figure 1). Shaded circles represent the
 233 possible lightning flash areas associated with each MAJIS frame (A,B,C,D labels
 234 corresponding to frame numbers 494, 504, 505, 506). The red-filled pixels indicate the location
 235 of maximum emission at 777 nm for each frame. The arrow highlights the direction of motion
 236 of MAJIS boresight and the time delay between detections.

237
 238 **Table 1 -** Properties of the frame-averaged MAJIS lightning spectra. Flash length represents
 239 the projected length of the MAJIS slit where lightning emissions are found.

flash	MAJIS frame	UTC start	Lon (°)	Lat (°)	flash length (km)
A	494	2024-08-20T21:26:48.47	95.64	6.19	28.2
B	504	2024-08-20T21:26:50.47	95.85	6.09	10.0
C	505	2024-08-20T21:26:50.67	95.86	6.08	12.0
D	506	2024-08-20T21:26:50.87	95.84	6.06	18.1

240
 241 The coverage of thermal emission by simultaneous MAJIS IR measurements enables
 242 understanding the context where lightning is observed. As highlighted in the papers by Poulet
 243 et al. (this issue) and Oliva et al. (this issue), thermal wavelengths can be used to evaluate
 244 optical thickness and top altitude of cloud systems. In our case, lightning appears located close

245 to a region having the lowest thermal emission in the whole data cube (i.e. the brightest feature
 246 in Figure 1 and Figure 3), revealing the presence of a very thick cloud. Although ice diagnostic
 247 signatures are mostly at solar-reflected wavelengths and hence not accessible in this case, the
 248 levels of brightness temperatures measured over this cloud is very similar to those found over
 249 ice-rich thick cloud systems in other daylight EGA cubes (Oliva et al., this issue), supporting its
 250 interpretation as a thunderstorm cloud. By using a representative nighttime vertical thermal
 251 profile (taken on 20 Aug 2024 in the nearest station at Banda Aceh¹), the brightness temperature
 252 measured by MAJIS (at a wavelength of 3979 nm, poorly absorbed by water vapour), can be
 253 converted into an estimate of the cloud top altitude. The result of this analysis is shown in Figure
 254 4. This indicates that most of the visible emission is concentrated just along the eastern edge
 255 of the thick cloud, whose top lies about 12 km above the surface. The detection near a cloud
 256 edge is easily explained by the differential absorption of scattered light inside the cloud, since
 257 the reduced optical thickness makes it easier for the lightning's light to escape into space
 258 through the cloud boundaries. As a possible analogue, we can refer to lightning images like that
 259 in the inset of Figure 4, captured from the orbiting International Space Station, at a spatial scale
 260 similar to MAJIS' one.
 261
 262



263
 264 **Figure 4:** MAJIS lightning emissions in the context of the clouds seen by MAJIS-IR. Grayscale
 265 surface shows the cloud top altitude retrieved from thermal emission at 3979 nm, labeled

¹ Data downloaded from Wyoming Weather Web, Upperair Air Data, station WITT 96011, University of Wyoming, <https://weather.uwyo.edu/upperair/>.

266 *using black contour lines. Green regions indicate the MAJIS pixels with lightning signatures*
267 *(maximum intensity in red areas), while pink shades are the corresponding circular areas*
268 *(same as in Figure 3). In the inset, a lightning flash imaged in 2021 from the International*
269 *Space Station, is used as an analogue of the MAJIS observation (Earth Science and Remote*
270 *Sensing Unit, NASA Johnson Space Center, Photo ID ISS066-E-24707). The horizontal*
271 *spatial scale (as indicated by the green arrow) is nearly the same in the two images.*
272

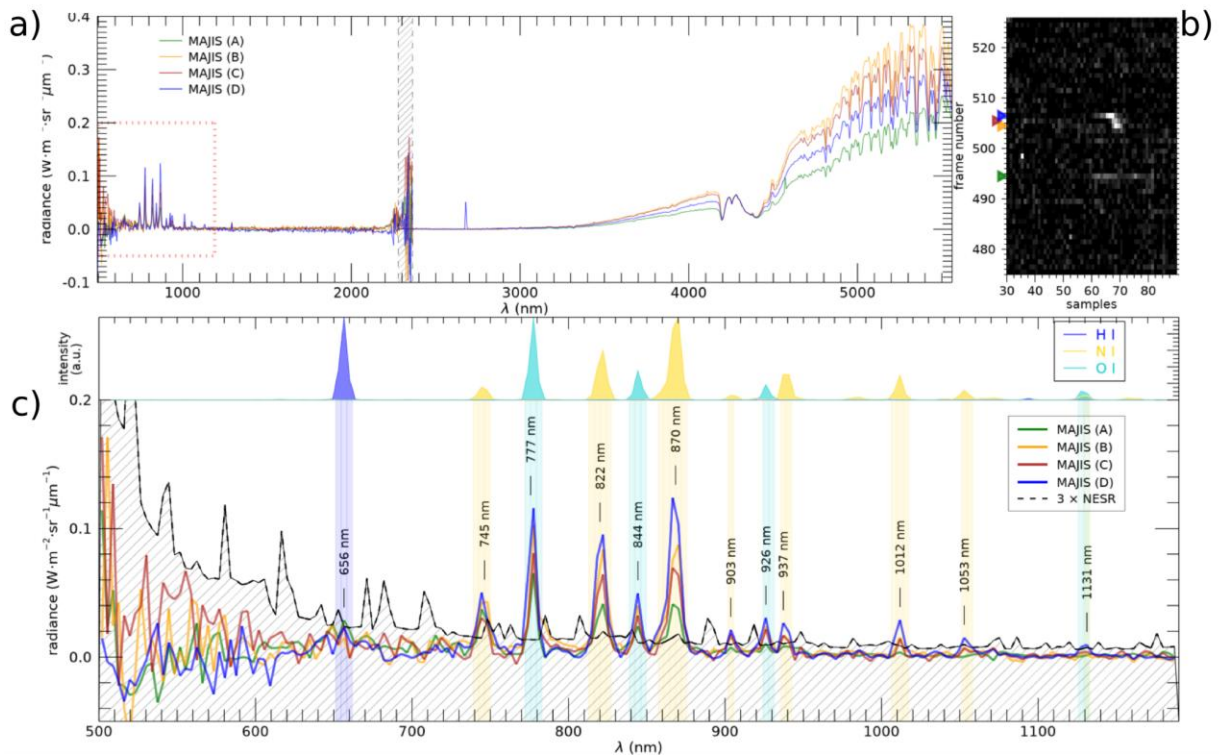
273 **2.3. Lightning spectral identification**

274
275 By averaging the spectra of different pixels within the same frame we obtain the 4
276 average spectra shown in Figure 5, corresponding to the parameters listed in Table 1. It is worth
277 stressing that, although small, the motion smearing has been taken into account when summing
278 adjacent spectra. In this case, a correction factor of $1/(1 + 2f) \sim 0.83$ is applied to the radiance
279 averaged along the slit, in order to avoid double-counting the signal coming from the overlapped
280 regions.

281 In Figure 5a the spectra are shown in the full MAJIS wavelength range, with the
282 boundary between the VISNIR and IR channels indicated around 2300 nm. Terrestrial thermal
283 emission dominates the signal longward ~ 3300 nm, spectrally shaped by the vertical profiles of
284 temperature and cloud/aerosols and water opacities, by the broad 4300 nm CO₂ band and by a
285 number of narrower water absorption bands in the 5000 nm range. The 500-1200 nm range,
286 blown up in Figure 5c, is characterized by a sequence of rather narrow lines, whose intensity is
287 quite variable from pixel to pixel. The main spectral feature in all spectra is represented by a
288 group of three lines (at 777 nm, 822 nm, and 870 nm), diagnostic of the presence of atomic
289 oxygen and nitrogen typical of terrestrial lightning (e.g. Orville et al., 1966). A series of weaker
290 but clear peaks is also observable at 745, 844, 903, 926, 937, 1012, 1053 and 1131 nm, but
291 with a more variable intensity. The spectra in Figure 5c are compared with a 3- σ noise level
292 (black curve), derived from background fluctuations after the correction described above
293 (Sect.2.1), which is used as a threshold for selecting the most significant emission lines (labeled
294 marks). A list of these lines along with the possible species contributing to them is compiled in
295 Table 2. Given the non-optimal resolutions (see Section 3), the presence of other minor
296 emission lines altering the spectral shapes cannot be totally excluded, but in principle no other
297 species/lines are needed to explain these observations. It is worth noting here that, although
298 the MAJIS instrument implements a powerful embedded despiking algorithm in its acquisition
299 pipeline (Langevin et al., 2020; Poulet et al., 2024b), it has not been used in these EGA
300 observations, meaning that the data can be affected by several spikes. This circumstance
301 proved favorable in our case, since the despiking processing could have erased or strongly
302 altered lightning signatures. In our case, the coexistence of several emission lines in the same
303 spectrum is the primary factor supporting the interpretation of the observations as lightning
304 emissions, intrinsically transient and localized, rather than ascribing them to spurious
305 instrumental spikes.

306 The largest SNR values, of the order of 20-25, are obtained for the O I 777 nm and N I
307 870 nm lines. As shown in the upper part of Figure 5c, the observed lines overall correlate with
308 those expected from atomic neutral nitrogen and oxygen, once they are calculated at
309 temperatures as high as thousands of kelvin. In this panel, the lines (shown for helping position
310 matching) are modeled on the basis of NIST Atomic Spectra Database (Kramida et al., 2024),
311 at a temperature of 6000 K in Local Thermal Equilibrium (LTE) conditions and then convolved
312 with the instrument line shape of the MAJIS VISNIR channel (gaussian response with 3.5-5.6
313 nm FWHMs and 3.6-3.7 nm/band sampling).

314 It is interesting to note that a faint peak, barely exceeding the 3- σ level, is also observed
 315 in MAJIS spectra at 656 nm, coincident with the atomic hydrogen H α . Even if this line is well
 316 known associated with lightning phenomena (Uman & Orville, 1964), its low SNR level prevents
 317 definite conclusions about the presence of hydrogen in MAJIS spectra. We cannot even rely on
 318 the presence of other lines of the Balmer series, all falling outside the MAJIS spectral range
 319 (e.g. H β at 486 nm). Further details on this analysis are given in Sect.4.4.
 320
 321



322 **Figure 5 - a)** MAJIS spectra averaged over the lightning pixels of the same frames (A,B,C,D),
 323 in the whole MAJIS spectral range. Emissions diagnostic of lightning are inside the dotted red
 324 box at left, blown up in panel c). The vertical dashed stripe around 2300 nm indicates the
 325 regions of spectral overlap between MAJIS VISNIR and IR channels. **b)** Section of the MAJIS
 326 visible image around lightning pixels (spectral average between 765 and 885 nm), with
 327 lightning frames highlighted by triangles at left. **c)** Lower part: Identification of emission lines
 328 detected in frame-averaged MAJIS lightning spectra. The labels highlight the wavelengths
 329 where the average signal exceeds the 3- σ level above noise (line-filled grey area). Upper part:
 330 Locations of the transitions expected by atomic nitrogen, oxygen and hydrogen, shown as a
 331 normalized intensity calculated in LTE condition at 6000 K (line parameters taken from NIST
 332 Atomic Spectra Database, version 5.12).
 333

334
 335 **Table 2 - Emission lines detected in MAJIS spectra.** The species most likely contributing to
 336 the observed lines are listed along other possible weaker contributors. The selection only
 337 includes the strongest transitions of main atmospheric constituents, on the basis of the
 338 closeness of an atomic transition to the MAJIS spectral band. Wavelengths in brackets, in
 339 nanometers, indicate the multiplet centers and are taken from the NIST database.

Observed position (nm)	most likely assignments	Additional contributions
------------------------	-------------------------	--------------------------

656.6	H I (656.3)	N I (660.3); N II (631.3); O II (656.6)
744.5	N I (746.9; 742.2; 743.7; 748.5)	N II (745.1)
777.7	O I (777.3); N I (772.8)	N II (776.2)
822.0	N I (816.6; 821.7); O I (822.2)	
844.3	O I (844.6)	H I (846.7; 843.8; 841.3; 839.2); N II (843.9); O II (837.6)
870.3	N I (868.1; 876.7; 866.4; 865.6)	H I (875.0; 866.5); N II (867.6; 868.7)
903.7	N I (906.1; 902.1; 904.7)	H I (901.5); N II (898.6); O II (900.6)
926.0	O I (926.4; 920.5); N I (918.7)	H I (922.9); O II (928.0); N II (921.7)
937.2	N I (941.9; 939.3; 946.4; 923.2)	N II (921.7; 940.0); O II (938.9)
1011.8	O I (1016.7); N I (1011.3; 1015.5)	
1052.8	N I (1053.9)	N II (1054.1; 1054.7)
1131	O I (1128.6; 1130.2); N I (1129.2)	

340

341

342

3. Modeling

343

344

345

346

347

Boggs et al., 2021):

348

$$I_{ji} = \beta \frac{g_j A_{ji}}{\lambda_{ji}} e^{-E_j/k_B T} \quad (1)$$

349

350

351

352

353

354

355

where λ_{ji} and A_{ji} are respectively the wavelength and the spontaneous emission Einstein coefficient of the $j \rightarrow i$ transition, g_j and the E_j are respectively the statistical weight and the excitation energy of the upper level, k_B is the Boltzmann constant and T the temperature. The factor $\beta = \gamma h c n_0 / Q(T)$ encloses all the quantities that are wavelength-independent, like the total number density n_0 of the atomic species and a scaling factor γ related to the observing geometry (h is the Planck constant, c the light speed and $Q(T)$ the partition function sum of the involved species).

356

357

358

Equation (1) represents the baseline for physically interpreting MAJIS lightning spectral features. Given that the factor β is independent of the transition, it cancels out in intensity ratios between lines of the same species.

359

360

361

362

It is important to note that MAJIS was not designed to measure lightning spectra, particularly in terms of spectral and temporal resolutions. Therefore, further considerations are presented in the following sections to better determine which quantities can be reliably retrieved from observations and their associated uncertainties (see sections 3.3 to 3.5).

363

364

3.1. Line widths and broadening

365

366

367

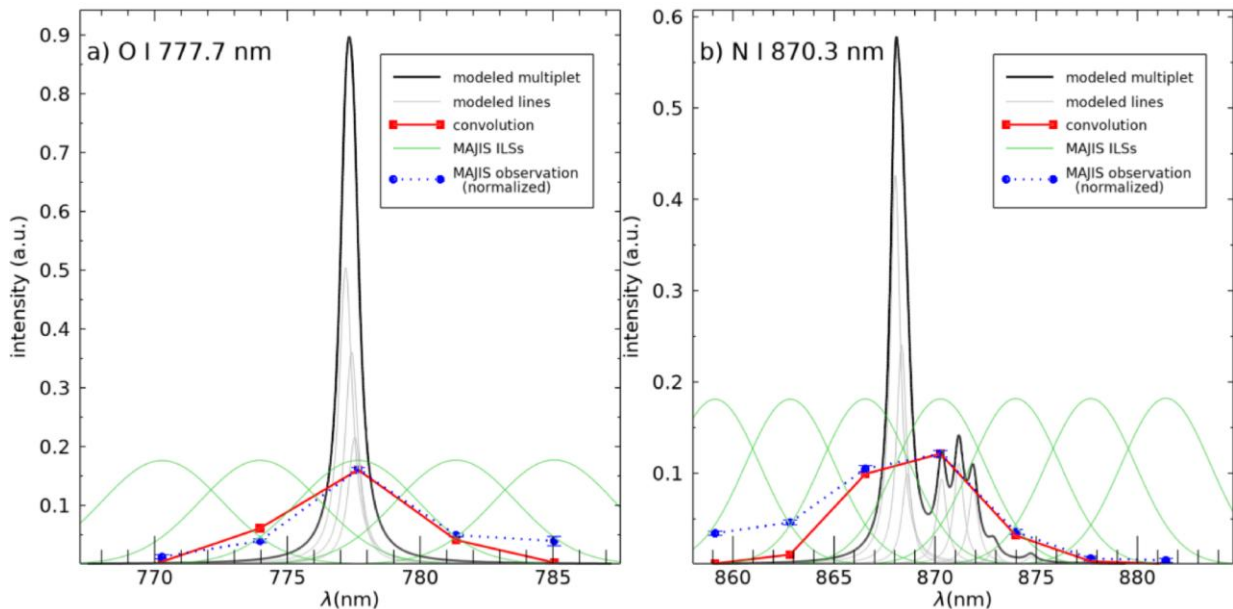
368

The presence of a rather strong electrical field makes the shape of the spectral lines emitted in lightning mainly broadened by the Stark effect (e.g. Gosse et al., 2025). In principle, this fact might offer a way for measuring the electron density in the lightning channel (Uman &

369 Orville, 1964). However, Stark-broadened FWHMs in lightning are estimated to be ≤ 0.3 nm
 370 (see e.g. Walker & Christian, 2019). Even if most of the emission lines are actually multiplets,
 371 i.e. they are composed of packed Stark-broadened lines slightly shifted with respect to each
 372 other, the expected multiplets width are usually $\lesssim 1$ nm.

373 In the cube under study, the spectral response of MAJIS pixels (Instrument Line Shape,
 374 ILS) is well described by Gaussian functions (Haffoud et al., 2024), with FWHMs of ~ 5.0 - 5.5 nm
 375 at wavelengths shorter than $1 \mu\text{m}$. On the other hand, the spectral sampling used in the lightning
 376 observations is ~ 3.7 nm, yielding a significant overlap between adjacent spectral bands. In any
 377 case, both quantities are larger than expected multiplet widths, which therefore fall well below
 378 the instrumental resolution capability.

379 Nevertheless, some of the stronger lines in MAJIS lightning spectra appear wider than
 380 one spectral point, but this can be readily interpreted as a consequence of the spectral
 381 instrumental sampling. As shown in Figure 6 for the cases of the two strongest lines (O I 777
 382 nm and N I 870 nm), the convolution of a theoretical multiplet spectral shape (black curves),
 383 with the MAJIS ILSs (green curves) makes the signal appear in distinct spectral points (red
 384 curves). This effect explains the general shape of the observed spectra (blue lines), which is
 385 therefore driven by the instrumental parameters rather than being an indication of a true line
 386 width, confirming that MAJIS observations cannot be used for measuring line broadening (and
 387 therefore electron density).
 388



389 **Figure 6** - Effect of the MAJIS spectral response on the shapes of emission lines, for the
 390 cases of O I 777 nm line (a) and N I 870 nm line (b). The initial, Stark-broadened, multiplet line
 391 (black curve) is modeled as a sum over individual lines (grey curves). Its convolution with
 392 MAJIS spectral response (Instrument Line Shapes, ILSs, shown as dashed green curves)
 393 yields a much broader line (red curve), explaining the wider signal seen in MAJIS lightning
 394 spectra (blue curves).
 395

396 3.2. Line intensity and spectral filling factors

397
 398
 399 MAJIS data have been calibrated in spectral radiance through Instrument Transfer
 400 Function (ITF), which provides the conversion between digital numbers and radiance values
 401 under the assumption that the whole spectral response width of a MAJIS pixel is fulfilled by the

402 incident light. In the lightning case, dealing with unresolved lines, this standard calibration does
 403 not correctly represent the true emission flux.

404 As a general scheme, we can think the MAJIS spectral radiance in a given band b , I_b ,
 405 characterized by a spectral width of $\Delta\lambda_b$, as the convolution of the source spectral radiance $R(\lambda)$
 406 with the MAJIS ILS $\Phi_b(\lambda)$ of that band:

$$407 \quad I_b = \frac{1}{\Delta\lambda_b} \int_{\Delta\lambda_b} R(\lambda)\Phi_b(\lambda)d\lambda \quad (2)$$

408 where the normalization factor is $\Delta\lambda_b = \int_{\Delta\lambda_b} \Phi_b(\lambda)d\lambda$.

409 If the source radiance is spectrally constant across the ILS spectral range, $R(\lambda) = R_c$, the
 410 MAJIS calibrated value is rigorous:

$$411 \quad I_b = \frac{1}{\Delta\lambda_b} \int_{\Delta\lambda_b} R_c\Phi_b(\lambda)d\lambda = R_c \quad (3)$$

412 On the contrary, the lightning radiances are emitted in narrow lines, as already discussed in
 413 Sect.3.1. We can think the radiance emitted by the source in a given line k as:

$$414 \quad R_k(\lambda) = R_{k,0}\rho_k(\lambda) \quad (4)$$

415 where the function $\rho_k(\lambda)$ represents a normalized adimensional spectral shape characteristic of
 416 the line k , evaluable *a priori* from line parameters, and $R_{k,0}$ the peak multiplet radiance. In the
 417 case of a multiplet composed of M Stark-broadened Lorentzian lines it will be:

$$418 \quad \rho_k(\lambda) = \frac{1}{\rho_M} \sum_{l=1}^M a_l \frac{w^2}{(\lambda-\lambda_l)^2+w^2} \quad (5)$$

419 where w is the Stark HWHM, λ_l the central wavelengths of the lines and a_l normalized weights
 420 related to line parameters. The normalization factor ρ_M can be chosen such that $max(\rho_k) = 1$,
 421 so that the quantity $R_{k,0}$ in equation (4) represents the peak radiance of the multiplet. In any
 422 case, by substituting (4) in (2), we can see that the source spectral radiance is proportional to
 423 the MAJIS calibrated value:

$$424 \quad R_{k,0} = I_b/\delta_{k,b} \quad (6)$$

425 where a spectral filling factor $\delta_{k,b}$ is defined as:

$$426 \quad \delta_{k,b} = \frac{\int \rho_k(\lambda)\Phi_b(\lambda)d\lambda}{\int \Phi_b(\lambda)d\lambda} \quad (7)$$

427 This also allows to retrieve the total radiance (in W/m²/sr) emitted from the line k in the
 428 MAJIS spectral band b as:

$$429 \quad R_{k,tot}(b) = I_b \frac{\int \rho_k(\lambda)d\lambda}{\delta_{k,b}} \quad (8)$$

430
 431 The MAJIS filling factors $\delta_{k,b}$ evaluated for the main oxygen and nitrogen lines are
 432 reported in Table 3 and Table 4 respectively, where we can see that most values fall in the
 433 range 0.1-0.3. It is important to stress that such factors depend on both indices k and b , being
 434 referred to the multiplet k viewed in MAJIS band b (adjacent bands can measure the same
 435 multiplet with different filling factors). Furthermore, these correction factors are of course model-
 436 dependent. In particular, they are dependent on the intrinsic line broadening assumed in
 437 modeling multiplets (we adopted a constant value $w = 0.3$ nm for all lines). On the other hand,
 438 the dependence on temperature is mitigated by the fact that the transitions inside the same
 439 multiplet take place between atomic configurations very similar in terms of energy, resulting in
 440 a negligible variation of $\delta_{k,b}$ factors with respect to T.

441

442 3.3. Oxygen lines

443

444 Emission lines diagnostic of atomic oxygen are clearly visible at 777.7 nm and 844.3 nm,
 445 in all MAJIS lightning spectra. A summary of the detected lines is reported in Table 3, including
 446 the values of spectral filling factors defined in the previous Sect.3.2. They are both produced by
 447 oxygen de-excitation through transitions $3p \rightarrow 3s$. The same levels are involved in the emission
 448 at 822 nm, also clearly observable, but not equally diagnostic being it overlapped with a strong
 449 nitrogen line. Another fainter oxygen line is seen at 926 nm, ascribed to $3d \rightarrow 3p$ transitions, that
 450 should also contribute to the even fainter feature seen at 1127.5 nm, yet uncertain in nature due
 451 to the closeness of a nitrogen line at 1129 nm.

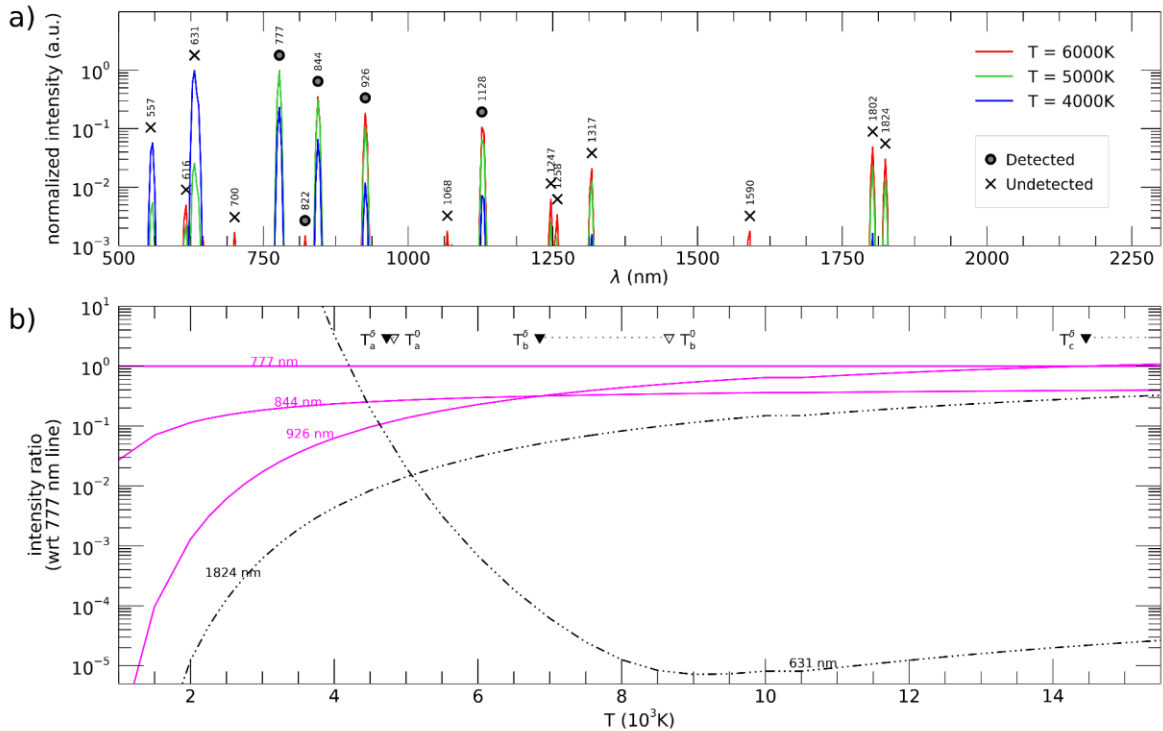
452 In Figure 7a, we can see simulations of the relative intensity of oxygen lines (with respect
 453 to 777 nm line) obtained through equation (1). Temperatures of ~ 5000 K are needed to populate
 454 the 3p and 3d levels enough to produce the observed emissions, but higher temperatures would
 455 increase the population of higher levels (in particular 4s, 4d, 4f, 5d, 5f) yielding stronger
 456 emissions at wavelengths where they are not observed at all (e.g. 616.6, 700.4, 1067.8, 1317.3,
 457 1590.5, 1802.6, 1824.5 nm). On the other hand, a decrease in temperature would make stronger
 458 emissions related to low energy transitions, such the green line at 557.73 nm and the red line
 459 at 631 nm (common in auroral phenomena at lower temperature, e.g. Ivenko et al., 2019) that
 460 are equally not observed in MAJIS spectra.

461 A comprehensive framework for constraining the temperature is presented in Figure 7b,
 462 where the relative intensities of the most significant emission lines are plotted as a function of
 463 temperature, also accounting for the spectral filling factors discussed in previous Sect.3.2. The
 464 non-detection of the 631 nm line implies its intensity must fall below that of 926 nm line, a
 465 condition that occurs for $T \geq 4700$ K (labeled T_a in the plot). At higher temperatures, the 1824 nm
 466 line is expected to exceed in intensity the 844 nm line (at $T \geq 22000$ K, not shown). Actually, a
 467 stronger upper constraint is provided by the crossing between the 777 nm and 926 nm lines,
 468 that implies $T \leq 14000$ K (T_c in the plot) to preserve the dominance of the 777 nm line. As a
 469 consequence, the oxygen line intensities are overall consistent with a broad temperature range
 470 of 4700-14000 K. It is noteworthy that neglecting the spectral filling factor correction would bias
 471 this conclusion, widening the confidence interval to 4800-20000 K (white triangles in Figure 7).
 472

473 **Table 3:** MAJIS emission features identified as O I emission lines, associated with the atomic
 474 transition expected to mainly contribute to the MAJIS line. The selection is based on the
 475 largest spectral overlap of an atomic line with the response of the given MAJIS spectral band
 476 (i.e. the largest spectral filling factor, last column), evaluated through equation (7) (line
 477 parameters from NIST database).

Observed line positions	Electronic transitions		Spectral filling factor
	nm	Line assignment	
777.7	777.34	$2s2.2p3.(4S^{\circ}).3s - 2s2.2p3.(4S^{\circ}).3p [5S^{\circ}-5P]$	0.18
822.0	822.20	$2s2.2p3.(2D^{\circ}).3s - 2s2.2p3.(2D^{\circ}).3p [3D^{\circ}-3D]$	0.27
844.3	844.65	$2s2.2p3.(4S^{\circ}).3s - 2s2.2p3.(4S^{\circ}).3p [3S^{\circ}-3P]$	0.15
926.0	926.39	$2s2.2p3.(4S^{\circ}).3p - 2s2.2p3.(4S^{\circ}).3d [5P-5D^{\circ}]$	0.22
1127.5	1128.6	$2s2.2p3.(4S^{\circ}).3p - 2s2.2p3.(4S^{\circ}).3d [3P-3D^{\circ}]$	0.15

478



479
 480 **Figure 7:** Calculated intensities for O I lines in the MAJIS VISNIR range at different
 481 temperatures, normalized to that of 777 nm line and corrected for spectral filling factor. **a)**
 482 Spectral distribution of strongest O I lines at three temperatures, labeled depending on their
 483 detectability in MAJIS spectra. **b)** Intensity ratios as a function of temperature, for selected O I
 484 lines, showing relative changes in a wider range of temperatures. Solid magenta curves
 485 represent detected lines, while dot-dashed black curves undetected ones. Significant
 486 intersection points are indicated by black-filled triangles: T_a (4730 K) between 631 nm and 926
 487 nm, T_b (6860 K) between 926 nm and 844 nm, T_c (13500 K) between 777 nm and 926 nm
 488 (white-filled triangles indicate the corresponding values without applying spectral filling factor).
 489

490 3.4. Nitrogen lines

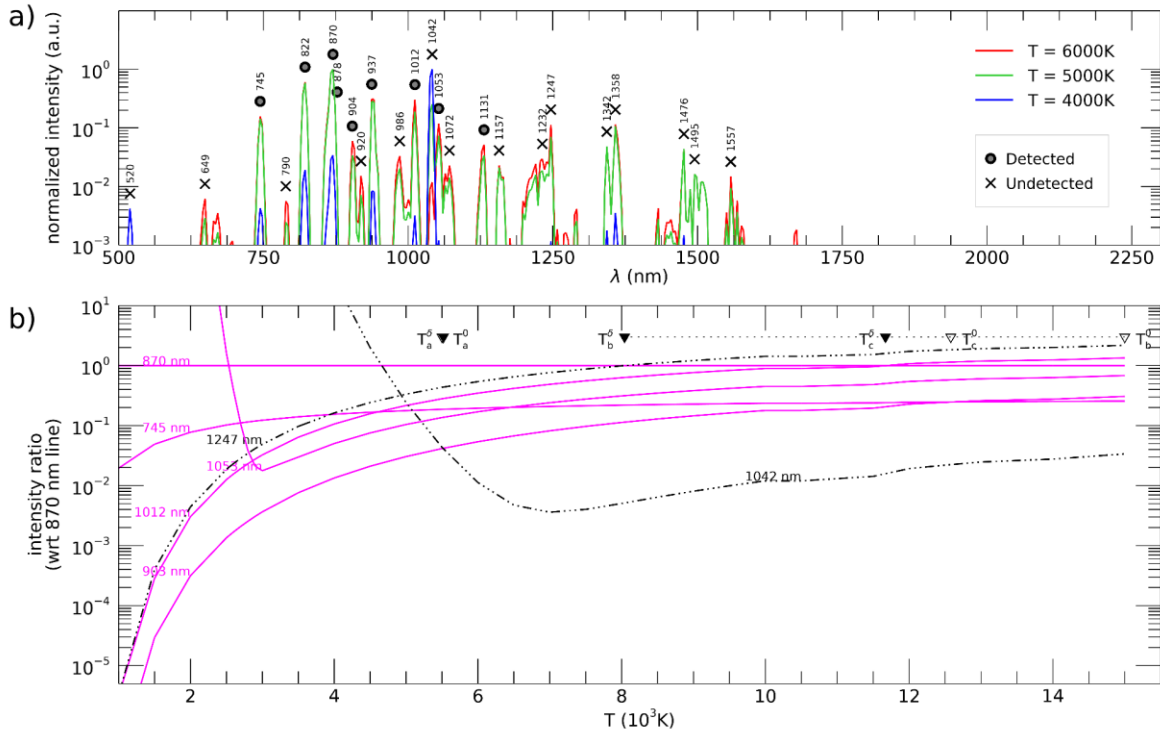
491
 492 Neutral atomic nitrogen is responsible for most features in MAJIS spectra as listed in
 493 Table 4. The stronger ones, found in all spectra, are at 745, 822, 870, 937 nm, and are all
 494 associated with transitions $3p \rightarrow 3s$. Other shallower lines are centered at 903, 1012, 1053, 1131
 495 nm, and should be ascribed to N I decay to the $3p$ level ($3d \rightarrow 3p$ and $4s \rightarrow 3p$).

496 As in the oxygen's case, a qualitative estimate of a temperature range compatible with
 497 the observations can be inferred by comparing them with model equation (1). Figure 8a,
 498 indicates increasing temperature yields stronger emissions at longer wavelengths, while no
 499 features are seen in MAJIS spectra for $\lambda > 1131$ nm. Although pertaining to the same $3p \rightarrow 3s$
 500 transition, no emission is found at 1353 nm, as well as at 790, 920 and 1073 nm. The same
 501 evidence applies to the missing 1232-1250 nm complex, related to other $3d \rightarrow 3p$ transitions.
 502 Finally, also in this case there are some lower-energy transitions, located near 520 and 1042
 503 nm, whose non-detection can constrain the minimum temperature.

504 As also done for oxygen (see previous Sect.3.3), a temperature plot for nitrogen is shown
 505 in Figure 8 b, including trends of relative intensities of most significant nitrogen lines (with
 506 respect to the 870 nm line). Again, a lower temperature boundary can be determined from the
 507 crossing of the 903 nm line with the undetected one at 1042 nm (labeled T_a in the plot), yielding

508 $T \gtrsim 5500$ K. Upper boundaries can be inferred from undetected lines at longer wavelengths, such
 509 as the 1247 nm, whose calculated intensity is larger than other detected lines. The crossing
 510 point between the 1247 nm line and the strongest 870 nm (T_b in the plot) would suggest $T \lesssim 8000$
 511 K, but this estimate is highly sensitive to the value of spectral filling factor (shifting to 15000 K if
 512 neglected). A more reliable upper boundary can be set by requiring that the intensity of the 1012
 513 nm line remains below that of 870 nm one, yielding $T \lesssim 12000$ K (T_c in the plot).

514 Hence, on this semiquantitative basis, the range of temperatures compatible with the
 515 nitrogen lines intensities (5500-12000 K) is also compatible with that derived from oxygen in the
 516 previous Sect.3.5 (4700-14000 K).
 517



518
 519 **Figure 8:** Calculated intensities for N I lines in the MAJIS VISNIR range at different
 520 temperatures, normalized to that of 870 nm line and corrected for spectral filling factor. **a)**
 521 Spectral distribution of strongest N I lines at three temperatures, labeled depending on their
 522 detectability in MAJIS spectra. **b)** Intensity ratios as a function of temperature, for selected N I
 523 lines, showing relative changes in a wider range of temperatures. Solid magenta curves
 524 represent detected lines, while dot-dashed black curves undetected ones. Significant
 525 intersection points are indicated by black-filled triangles: T_a (5520 K) between 903 nm and
 526 1042 nm, T_b (12620 K) between 903 nm and 745 nm, T_c (11670 K) between 1012 nm and 870
 527 nm (white-filled triangles indicate the corresponding values without applying spectral filling
 528 factor).
 529

530 **Table 4 - Same as Table 3 but for N I.**

Observed line positions	Electronic transitions		Spectral filling factor
	nm	Line assignment	
745.5	745.22	2s2.2p2.(3P).3s - 2s2.2p2.(3P).3p [4P-4S ^o]	0.21

	740.65	2s2.2p2.(3P).3s - 2s2.2p2.(3P).3p [4P-2D°]	0.26
822	821.18	2s2.2p2.(3P).3s - 2s2.2p2.(3P).3p [4P-4P°]	0.29
862.8	865.95 866.44	2s2.2p2.(3P).3s - 2s2.2p2.(3P).3p [2P - 2P°] 2s2.2p2.(1D).3s - 2s2.2p2.(3P).5p [2D - 2P°]	0.20 0.21
866.5	866.44	2s2.2p2.(3P).3p - 2s2.2p2.(3P).3d [2S° - 2D]	0.15
870.3	869.16	2s2.2p2.(3P).3s - 2s2.2p2.(3P).3p [4P-4D°]	0.21
877.7	876.13	2s2.2p2.(3P).3p - 2s2.2p2.(3P).3d [2S° - 4D]	0.18
903.7	902.07 904.99	2s2.2p2.(3P).3p - 2s2.2p2.(3P).3d [2S° - 4F] 2s2.2p2.(3P).3p - 2s2.2p2.(3P).3d [2S° - 2P]	0.12 0.17
937.2-941.0	936.00 939.53 941.94	2s2.2p2.(1D).3p - 2s.2p4 [2D* - 2D] 2s2.2p2.(3P).3s - 2s2.2p2.(3P).3p [2P-2D°] 2s2.2p2.(3P).3s - 2s2.2p2.(3P).3p [2P - 4S*]	0.15 0.16 0.14
1011.8	1011.68	2s2.2p2.(3P).3p - 2s2.2p2.(3P).3d [4D°-4F]	0.24
1015.5	1011.68	2s2.2p2.(3P).3p - 2s2.2p2.(3P).3d [4D* - 2P]	0.17
1052.8	1052.63	2s2.2p2.(3P).3p - 2s2.2p2.(3P).3d [4P* - 4D]	0.30
1127.5	1125.73	2s2.2p2.(1D).3p - 2s.2p4 [2P* - 2D]	0.12
1131.2	1128.86	2s2.2p2.(3P).3p - 2s2.2p2.(3P).4s [4D* - 4P]	0.23

531

532

533

3.5. Temporal resolution

534

535

536

537

538

539

540

541

542

543

544

545

546

547

548

549

550

551

As far as time is concerned, lab studies of triggered lightning show that light pulses raise to a maximum intensity in time scales of 0.5-1.5 μs , then to decrease exponentially with a longer decay time τ of the order of 10-100 μs (e.g. Walker & Christian, 2019; Kieu et al., 2019). Analogous to the spectral case discussed above (Sect.3.2), the radiance value from the standard MAJIS calibration refers to an integration time ($t_{int} = 22 \text{ ms}$) that is possibly much longer, and is therefore not representative of the true radiance emitted by the source. If we consider the simplest case of a single pulse event with a decay time τ , of the form:

$$R(t) = R_{peak} e^{-t/\tau} \quad (9)$$

the MAJIS radiance, given by the time integration up to t_{int} , will be:

$$I_{MAJ} = R_{peak} \frac{t_{int}}{\tau} (1 - e^{-t_{int}/\tau}) \approx \frac{t_{int}}{\tau} R_{peak} \quad (10)$$

where last term holds if $\tau \ll t_{int}$. The peak radiance can therefore be retrieved from MAJIS values by applying a temporal filling factor δ_t :

$$R_{peak} = I_{MAJ}/\delta_t \quad \text{with} \quad \delta_t = \frac{\tau/t_{int}}{1 - e^{-t_{int}/\tau}} \approx \frac{\tau}{t_{int}} \quad (11)$$

In this simplified model, no instrument noise has been accounted for, making the signal decay to zero. In a more realistic case, during the integration time the emission does not contribute anymore to the signal after dropping below the noise level, and the expression for R_{peak} changes to:

$$R_{peak} = (I_{MAJ} - NESR)/\delta_t \quad (12)$$

Anyway, contrary to the spectral filling factor, the evaluation of δ_t is much more difficult since we do not know *a priori* the temporal behaviour of the lightning flash. Decay times for individual lines are provided by some lab measurements of triggered lightning, spanning a large range of values. E.g. Walker & Christian (2019) report values $\tau \sim 140 \mu\text{s}$ for the N I 745 nm line, while much shorter decay time ($\tau \sim 18 \mu\text{s}$) can be inferred from data in Kieu et al. (2019) for the OI 777 nm line. If these times are considered in equation (11), the resulting peak radiance at 745 nm and 777 nm would be 160 and 1200 times larger than MAJIS standard ones, respectively. But lightning flashes are rarely composed of single pulses and they rather consist of clustered sequences of pulses, separated from dozens to hundreds of milliseconds, making the light emission to last as a whole for much longer times (>100-200 ms), possibly even larger than the MAJIS integration time (López et al., 2017; Peterson & Rudlosky, 2019).

A second order effect related to the poor temporal resolution can also occur for lines having the same decay time but different strength. In this case, during the integration time the contribution to the signal due to the weaker line drops below that due to background noise earlier in time with respect to a stronger line. Therefore, a different distance from the noise level can bias the lines ratio, and possibly temperature retrievals (see Sect.4.2).

A further source of uncertainty is related to the large temporal gaps between MAJIS acquisitions: subsequent frames start 200 ms apart but the signal is integrated for 22 ms only, leaving 178 ms gaps in between. Therefore, we have no information not only on the number of strokes occurring but also if detectable flashes were shorter or longer than 22 ms and which portion of their lifetime is sampled by MAJIS acquisitions or fall in the gaps instead.

These considerations can imply large variations, even by orders of magnitude, in estimating the lightning emission intensity from MAJIS data. In order to better constrain these aspects, we attempted to find detections of the same lightning events from either on-ground stations networks or other satellites, eventually providing independent insights on timing and intensities, but without success (more details on this in Sect.4.4).

Given the large amount of uncertainty related to this aspect, a value $\delta_t = 1$ has been used for the radiances previously reported in Figure 7 and Figure 8, while further consequences of temporal resolution will be discussed in Sect.4.2.

4. Discussion

4.1. The MAJIS observation in the context of lightning spectroscopy

After a few pioneering works in the 19th century (e.g. Joule, 1872), the spectroscopy of atmospheric lightning was boosted from the 1960s, when fast slitless spectroscopy enabled the identification of several spectral lines in the UV to visible range in individual flashes (e.g. Salanave et al. 1962, 1964; Krider, 1965; Orville, 1966). These time-resolved observations succeeded in identifying atomic and singly-ionized nitrogen lines, as well as atomic oxygen and hydrogen, and in estimating temperature and electron density in the discharge channel (Prueitt, 1963; Krider, 1973; Li et al., 2016; Boggs et al., 2021; Xu et al., 2024). A number of lab experiments reproducing natural lightning conditions (triggered lightning) have also been conducted in the subsequent decades (e.g., Larigaldie et al., 1981; Barvir et al., 2004; Li et al., 2016; Carvalho et al., 2018; Walker & Christian, 2019; Kieu et al., 2020), allowing more accurate and controlled studies of the discharge processes. Other observations stressed the production of other chemical species triggered by lightning, such as nitrogen oxides or carbon compounds

599 (Franzblau & Popp, 1989; Jadhav et al., 1996; Langford et al., 2004; Kieu et al., 2021). Overall,
600 most recent investigations increased the relevance of lightning in atmospheric physics and
601 chemistry, by stressing its triggering role for other transient events in the upper atmosphere (like
602 sprites, blue jets, and gamma-ray flashes) and the subsequent non-equilibrium atmospheric
603 chemistry providing a possible source of important greenhouse gases such O₃ or N₂O (see e.g.
604 Gordillo-Vázquez & Pérez-Invernón, 2021, and references therein).

605 Modern spectroscopic techniques enabled lightning observations at frame rates as high
606 as 1 MHz or more, with exposure times as short as 0.5 μs. Current knowledge assumes peak
607 temperatures of the discharge channel around 40000 K during the first few microseconds of the
608 lightning return stroke, with a spectrum composed of hydrogen from disassociated water and
609 singly/doubly ionized lines of atomic atmospheric constituents (i.e. nitrogen, argon, oxygen).
610 Then, a cooling period follows, reaching temperatures in the 20000 K range tens of
611 microseconds after the onset, and with spectra only consisting of neutral atomic emission lines,
612 followed by a slow decrease of line intensities and temperature until signal disappearance over
613 the course of milliseconds. In the longer cooling phase, molecular reactions involving NO_x can
614 occur, even if some authors report anomalously high NO/NO_x ratios for several minutes
615 (Franzblau & Popp, 1989).

616 All the cited spectroscopic observations of terrestrial lightning have been conducted from
617 the ground. On the other hand, space-based observations dedicated to lightning studies usually
618 rely on large-field imaging in narrow spectral filters, often aimed at the 777 nm O I line in the
619 visible spectrum, like the data provided by LIS (Lightning Imaging Sensor, Christian et al., 2003),
620 ASIM (Atmosphere Space Interaction Monitor, Pérez-Invernón et al., 2022), or GLM
621 (Geostationary Lightning Mapper, Goodman et al., 2013) instruments, to name a few. These
622 datasets are optimal for either global or regional statistical studies, like lightning climatology and
623 flash rates (e.g. Cecil et al., 2014), ratio of cloud-to-ground to intracloud flashes (e.g. Boccippio
624 et al., 2001), their relationship with mixed-phase precipitation (e.g. Petersen et al., 2005), or
625 their link with terrestrial gamma ray flashes (e.g. Barnes et al., 2015; Gjesteland et al., 2017).
626 On the other hand, spectral extensions of space-based observations to the blue/ultraviolet
627 spectral range (like the 180 and 337 nm spectral bands of ASIM) proved useful for improving
628 the physical understanding of blue flashes and elves (Li et al., 2021; Li et al., 2023; Bai et al.,
629 2023; Bjørge-Engeland et al., 2024).

630 Lightning is also of great interest for other planetary atmospheres in the Solar System
631 and beyond, with evidence having been accumulated over the years on many planets (see Aplin
632 & Fischer, 2017, for a review). The first detection on Jupiter dates back to the Voyager 1
633 encounter (Gurnett et al., 1979), followed by confirmations by the Cassini (Dyudina et al., 2004)
634 and Juno (Kolmašová et al., 2018; Brown et al., 2018; Imai et al., 2019; Becker et al., 2020;
635 Kolmašová et al., 2023a) spacecrafts. Data from the Voyager probes allowed inference of
636 lightning on the other giant planets, i.e. on Saturn (Warwick et al., 1982), then firmly assessed
637 by Cassini spacecraft (Fischer et al., 2006), on Uranus (Zarka & Pedersen, 1986), and on
638 Neptune (Gurnett et al., 1990). In many of these cases, electrical discharges have been
639 identified thanks to their radio and microwave emissions, and sometimes through visible
640 imaging of possible flashes associated with thick cloud structures. On Venus, preliminary
641 insights of lightning processes were not confirmed by in-depth scrutiny of imaging spectrometry
642 datasets by Venus Express (Cardesín Moinelo et al., 2016), leaving the occurrence of lightning
643 on this planet still debated (Lorenz, 2018). The only evidence of transient luminous events
644 registered by a spectrometer has been reported at Jupiter by the Juno UV spectrograph,
645 although the observed spectra, dominated by H Lyman band emission at 160 nm and hence

646 very similar to Jovian auroral emissions, could be ascribed to events occurring above the Jovian
 647 clouds, like sprites or elves (Giles et al., 2020).

648

649 **4.2. Emitted energy**

650

651 The strongest single-pixel intensities registered by MAJIS in lightning spectra are found
 652 in the oxygen line at 777 nm (max radiance of $0.418 \text{ W/m}^2/\text{sr}/\mu\text{m}$) and in the nitrogen line at 870
 653 nm (max radiance of $0.374 \text{ W/m}^2/\text{sr}/\mu\text{m}$), both within the flash D (Figure 5).

654 As discussed in Sect.3, these radiance values do not represent the emitted source
 655 radiance, being biased by resolution effects. Dimensionless filling factors can be introduced to
 656 attempt recovering the emitted radiances:

$$657 R_{kb} = I_b / (\delta_s \cdot \delta_{t,kb} \cdot \delta_{\lambda,kb}) \quad (13)$$

658 Here R_{kb} is the radiance emitted in the line k and measured in MAJIS band b , I_b is the
 659 MAJIS standard-calibrated radiance, and δ_s , $\delta_{t,kb}$, $\delta_{\lambda,kb}$ are the spatial, temporal and spectral
 660 filling factors respectively. However, spatial and temporal filling factors are only relevant if
 661 dealing with specific quantities such as radiance, but they are not needed to derive the total
 662 energy impinging the detector. As the lightning flashes are the only sources of photons, MAJIS
 663 signal is already proportional to the lightning flux integrated over the pixel's footprint and flash
 664 duration, and only the spectral filling factor $\delta_{\lambda,kb}$ has to be applied to retrieve the emitted
 665 radiance. In other words, by taking advantage of equation (8), if the emission line k is covered
 666 by the MAJIS band b , the measured energy density, per unit area and solid angle, is $D_k =$
 667 $R_{k,tot}(b) t_{int}$ (in $\text{J/m}^2/\text{sr}$), which is a quantity comparable with other observations being
 668 independent on instrumental parameters. In the further assumptions that this energy density is
 669 uniform over the whole flash area Σ_f (i.e. the circular regions introduced in Sect.2.2) and that
 670 the light of the discharge, isotropically emitted by lightning, is fully backscattered by clouds
 671 towards the detector with negligible loss, we can evaluate the total energy E_k emitted by a
 672 lightning in the line k as:

$$673 E_k = D_k 4\pi \Sigma_f = R_{k,tot}(b) t_{int} 4\pi \Sigma_f \quad (14)$$

674 The values of D_k and E_k obtained for the strongest lines O I 777 nm and N I 870 nm are
 675 summarized in Table 5, associated with statistical uncertainties, of the order of 25%, derived
 676 from error propagation of MAJIS uncertainties.

677 The values at 777 nm are particularly useful for comparing MAJIS observations with
 678 other datasets, since this line is routinely monitored by satellite observations devoted to
 679 lightning. Our derived energy densities are compatible with flash radiances reported in literature
 680 for average-intensity lightning. If early airborne observations reported 90% flashes having
 681 energy larger than $5 \cdot 10^{-6} \text{ J}\cdot\text{m}^{-2}\cdot\text{sr}^{-1}$ (Christian & Goodman, 1987), modal values obtained from
 682 LIS statistics range around $0.5 \text{ J}\cdot\text{m}^{-2}\cdot\text{sr}^{-1}\cdot\mu\text{m}^{-1}$ (corresponding to $\sim 5 \cdot 10^{-4} \text{ J}\cdot\text{m}^{-2}\cdot\text{sr}^{-1}$ once a line width
 683 of the order of 1 nm is taken into account, see Köhn et al., 2024, their figure 8), which is a value
 684 only 5 times higher than those in Table 5. The total energy released through this line ranges
 685 between 140 and 700 kJ in MAJIS observations, but if we consider the frames B, C and D as
 686 part of a single flash (spread over the largest D area and spanning a total time of 422 ms, not
 687 far from the average 345 ms flash duration over ocean, see e.g. Rudlosky et al., 2019), the
 688 integrated energy rises to $\sim 1.3 \text{ MJ}$. These values reside near the lower boundary of global
 689 statistics, which spans from 1 MJ for small flashes to $>10 \text{ GJ}$ for superbolts (e.g. Peterson,
 690 2023). Anyway, it is worth keeping in mind that the values we inferred depend on assumptions
 691 about areal and angular integration that are not well constrained and the E_k values can represent
 692 a lower limit of the actual flash energy. As stressed by systematic comparisons of ground- and

693 space-based lightning observations, the energy seen from space can be significantly lower than
 694 that measured from ground, probably due to the fact that most of the optical energy emitted by
 695 a return stroke comes from its portion near the ground, hence considerably absorbed by
 696 overlying clouds (Wemhoner et al.2026).

697
 698 **Table 5** - Intensity of main oxygen and nitrogen emissions for the four flashes registered by
 699 MAJIS. I_b is the frame-averaged radiance from the standard calibration pipeline; D_k is the
 700 corresponding energy density, while E_k is the lightning emitted energy under the assumption of
 701 equation (14), extrapolated to a minimal flash area Σ_f . The last row reports the total energy
 702 emitted by B, C, D flashes as pertaining to a unique sequence, assuming their average energy
 703 density spread over the whole area of the largest frame D).

flash	Σ_f	OI 777 nm line			NI 870 nm line		
		I_b	D_k	E_k	I_b	D_k	E_k
	km ²	W·m ⁻² sr ⁻¹ μm ⁻¹	10 ⁻⁵ J·m ⁻² sr ⁻¹	kJ	W·m ⁻² sr ⁻¹ μm ⁻¹	10 ⁻⁵ J·m ⁻² sr ⁻¹	kJ
A	624	0.07 ± 0.02	8.9 ± 2.2	700 ± 170	0.04 ± 0.01	6.8 ± 2.4	540 ± 180
B	79	0.10 ± 0.02	14.0 ± 3.2	140 ± 30	0.09 ± 0.02	16.0 ± 4.1	160 ± 40
C	113	0.12 ± 0.03	11.0 ± 2.8	160 ± 40	0.06 ± 0.02	12.0 ± 3.5	170 ± 50
D	256	0.12 ± 0.03	16.0 ± 3.5	510 ± 110	0.10 ± 0.02	19.0 ± 4.4	600 ± 140
sequence {B,C,D} (see caption)				1330±300			1500±380

704
 705
 706 **4.3. Temperature**
 707
 708 In sections 3.3 and 3.4 we deduced broad ranges of temperatures compatible with
 709 MAJIS lightning observations (corrected for spectral resolution only) from qualitative
 710 considerations on oxygen and nitrogen emissions, appearing in agreement with each other at
 711 least on order of magnitude (4700-14000 K from oxygen, 5100-11700 K from nitrogen). We
 712 investigate here two alternative methods for constraining the temperature in a more quantitative
 713 way.

714
 715 **4.3.1. Method 1: intra-species line ratios**
 716

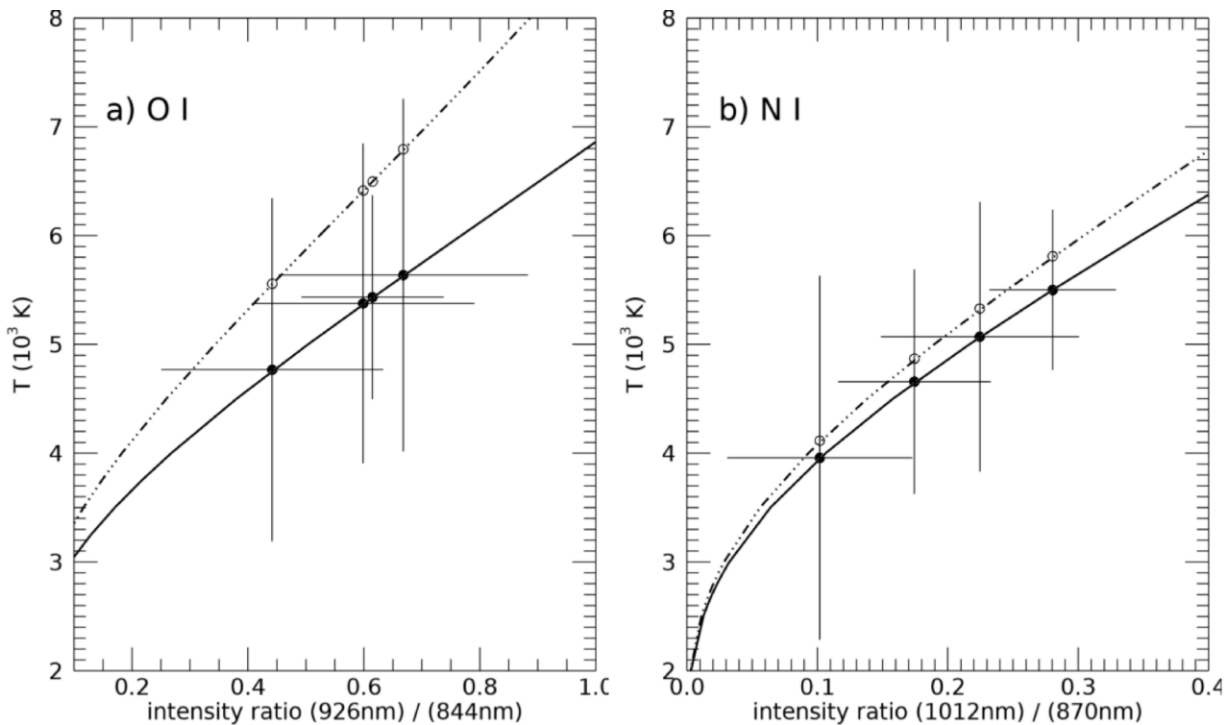
717 If we consider two multiplet transitions $j \rightarrow i$ and $m \rightarrow n$ of the same species, both
 718 described by equation (1), the radiance ratio of the two MAJIS bands covering them, I_b and I_q
 719 respectively, can be expressed as:

$$720 \quad T = \frac{E_m - E_j}{k_B} \left[\ln \left(\frac{\lambda_{ji} g_m A_{mn} \delta_{t,q} \delta_{\lambda,q} I_b}{\lambda_{mn} g_j A_{ji} \delta_{t,b} \delta_{\lambda,b} I_q} \right) \right]^{-1} \quad (15)$$

721 Here the radiances are expressed through equation (13), where only the spectral filling factors
 722 have been included.

723 This approach is widely adopted for measuring lightning channel temperature when
 724 dealing with spectrally- and temporally-resolved measurements of both natural and triggered
 725 lightning (e.g. Li et al., 2016; Kieu et al., 2021; Boggs et al., 2021). For MAJIS, the application
 726 of this equation is limited to bands covering one single multiplet, hence we selected the 844 nm
 727 and 926 nm lines in the case of oxygen, while the 870 nm and 1012 nm lines were chosen for
 728 nitrogen. Under the assumption that each pair of selected lines shares the same decay time (i.e.
 729 $\delta_{t,q}/\delta_{t,b} = 1$), we obtain the results summarized in Figure 9 and Table 6. The associated
 730 uncertainties are largely dominated by MAJIS measurement errors, whereas uncertainties in
 731 the multiplet parameters are considered negligible in this context (see e.g. Kramida, 2024, for a
 732 comprehensive review on uncertainties of atomic spectral lines, while the NIST database can
 733 be consulted for complete references' list on the subject).

734 All the obtained temperatures are rather similar, given also the high uncertainty levels
 735 (~20-30%). Those retrieved from nitrogen (4800 ± 1200 K on average) are systematically lower
 736 by a small amount (~2-15%, not statistically significant) than those from oxygen (5300 ± 1400 K
 737 on average). In the same Figure 9 the effect of spectral resolution is also shown (dash-dotted
 738 curve), revealing that the temperatures retrieved without correction are systematically higher.
 739 The effect is more pronounced in the oxygen case (usually characterized by narrower multiplets)
 740 where it amounts to ~20% (lower than 5% for nitrogen), but still small with respect to
 741 uncertainties.
 742
 743

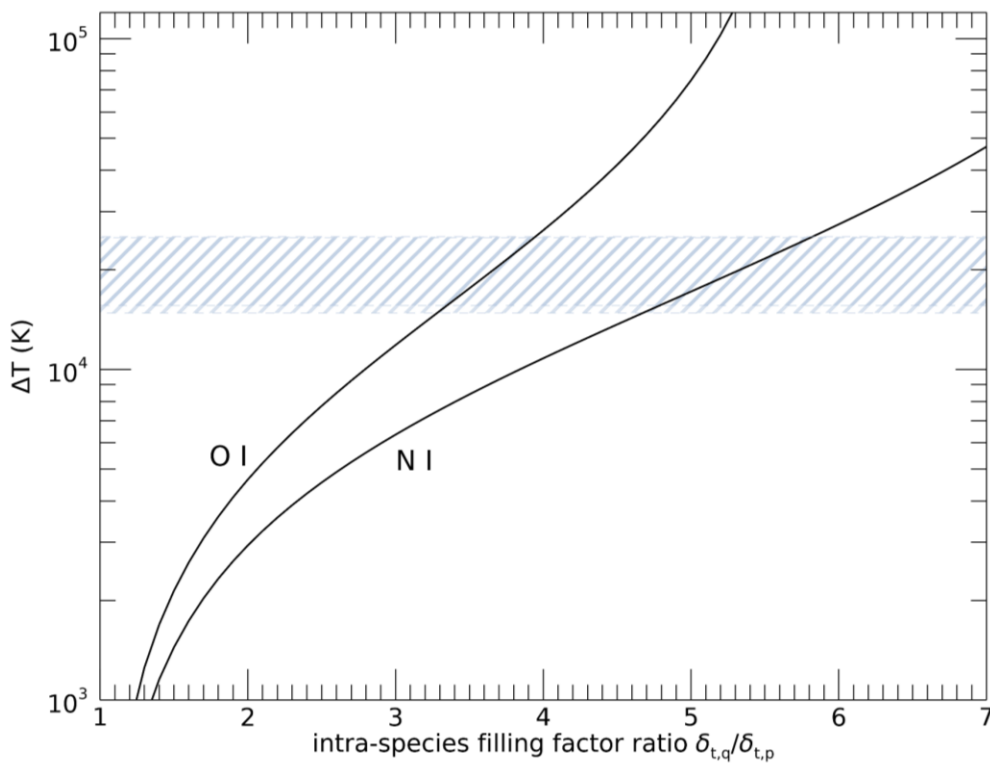


744 **Figure 9-** Lightning channel temperatures for the 4 MAJIS flashes, retrieved from the ratios of
 745 lines 926 nm and 844 nm for oxygen (panel a) and 1012 nm and 870 nm for nitrogen (panel
 746 b). Solid points with error bars show the retrieved values accounting for the spectral filling
 747 factor correction, whose temperature values are reported in Table 6. White points on the dash-
 748 dotted curve refer to the uncorrected MAJIS radiance values.
 749
 750

751 In any case, MAJIS observations suggest lightning channel temperatures of the order of
 752 5000 K, on the lower edge of the range of temperatures for natural lightning reported in literature.

753 For example, temperatures up to 15000-25000 K are found by Boggs et al. (2021) by using the
 754 ratio of oxygen lines at 777 nm and 716 nm (undetected by MAJIS). Temperatures up to 30000
 755 K were derived from observations of ionized nitrogen emissions (Orville, 1968), known to last
 756 for even shorter times at the beginning of a flash. Anyway, lightning channel temperature is
 757 related to its electrical current (Li et al., 2016), and colder events can occur on the top of the
 758 cloud, like streamer-like discharges and narrow bipolar events (Liu et al., 2021). Even if such
 759 events do not show evidence of emission at 777 nm, we cannot exclude that MAJIS
 760 observations encompassed different types of transient luminous events at different
 761 temperatures, further altering the ratios of observed line intensities.

762 A possible source of bias in our temperature estimation may be related to the uncertainty
 763 on the ratio of temporal filling factors $\delta_{t,q}/\delta_{t,b}$ in both oxygen and nitrogen cases. The inverse
 764 log dependence of the temperature on this ratio in equation (15) makes the retrieval very
 765 sensitive to this poorly constrained quantity. This sensitivity is represented in Figure 10, where
 766 the large offset of temperatures resulting from rather small variation of $\delta_{t,q}/\delta_{t,b}$ can be
 767 appreciated for both oxygen and nitrogen cases.
 768



769 **Figure 10-** Sensitivity of the temperature derived from equation (15) to the ratio of temporal
 770 filling factors, for both oxygen and nitrogen cases (same emission lines of Figure 9). Y axis
 771 represents the offset of temperature with respect to the case $\delta_{t,q}/\delta_{t,b} = 1$. Line-filled area
 772 indicates the offset range needed to match the temperatures from method 2 (inter-species
 773 ratios, see Sect.4.2.2).
 774
 775

776 4.3.2. Method 2: inter-species (oxygen to nitrogen) line ratios

777
 778 Another way to infer lightning temperature involves modeling the intensity ratios of
 779 oxygen lines with respect to the nitrogen ones. In this case, the β factor in equation (1) does not
 780 cancel out, and the ratio of the number densities and partition function sums have to be treated

781 explicitly. If we assign the $j \rightarrow i$ transition to an oxygen line (e.g. at 777 nm) and the $m \rightarrow n$ to a
 782 nitrogen line (e.g. 870 nm), we can keep the same notation of (15) and solve for the number
 783 density ratio to have:

$$784 \quad \frac{n_O}{n_N} = \frac{I_b(O) \delta_{\lambda,q} g_j A_{ji} \lambda_{mn} Q_O(T)}{I_q(N) \delta_{\lambda,b} g_m A_{mn} \lambda_{ji} Q_N(T)} e^{\frac{E_m - E_j}{kT}} \quad (16)$$

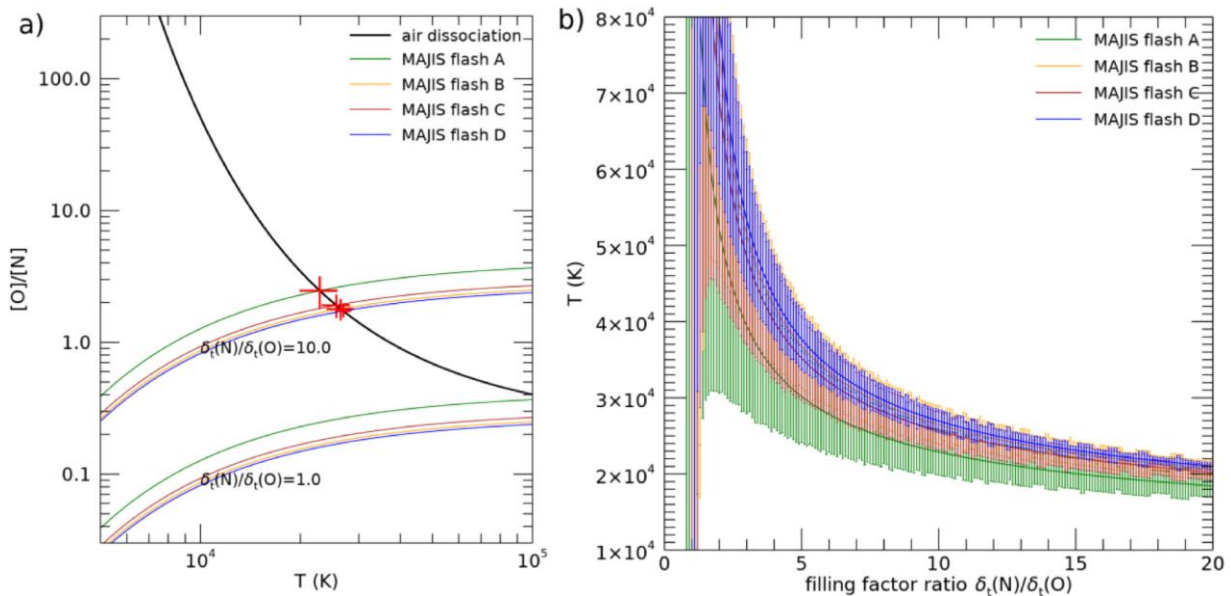
785
 786 In the Earth's atmosphere, atomic nitrogen and oxygen are dissociation products of
 787 molecular N_2 and O_2 , the most abundant and stably mixed molecules. Further contribution to
 788 oxygen can also come from H_2O dissociation. The ratio of atomic abundances can therefore be
 789 derived by evaluating the relative dissociation of these molecules at a given temperature.
 790 Including both O_2 and water dissociation, we can write:

$$791 \quad \frac{n_O}{n_N} = \chi_{O_2} e^{\frac{D_{N_2} - D_{O_2}}{k_B T}} + \frac{1}{2} \chi_{H_2O} e^{\frac{D_{N_2} - D_{H_2O}}{k_B T}} \quad (17)$$

792 where $\chi_{O_2} = n_{O_2}/n_{N_2}$ and $\chi_{H_2O} = n_{H_2O}/n_{N_2}$ represent the molecular mixing ratios, while D_{N_2} ,
 793 D_{O_2} , D_{H_2O} their dissociation energy. This equation provides a theoretical argument to be
 794 compared with the ratio derived from MAJIS observations in equation (16).

795 By evaluating equation (17) with mixing ratios $\chi_{O_2}=0.21$ and $\chi_{H_2O}=0.05$ (Cox, 2002) and
 796 dissociation energies $D_{N_2}=945$ kJ/mol (Frost & McDowell, 1956), $D_{O_2}=498$ kJ/mol (Wang et al.,
 797 2024), $D_{H_2O}=498$ kJ/mol (Darwent, 1970) yields the black curve in Figure 11a. This curve has
 798 to be compared with the ratio obtained through equation (16) by MAJIS data, shown in the same
 799 figure. In the calculation, a ratio of partition functions $Q_O(T)/Q_N(T) = 4$ is assumed, constant in
 800 the temperature range of interest, while line parameters are still taken from the NIST database.

801 The intensity ratio in equation (16) implies the presence of the temporal filling factor ratio,
 802 $\delta_t(N)/\delta_t(O)$, whose value cannot be easily constrained. If we let it as a free parameter, equation
 803 (16) provides a family of curves, as shown in Figure 11a for two values of $\delta_t(N)/\delta_t(O)$. Then,
 804 by solving for temperature (by equating (16) and (17)) we obtain a family of solutions for each
 805 flash detected, illustrated in Figure 11b (error bars are derived from propagation of the MAJIS
 806 radiance uncertainties). We can see that, whatever is the value of $\delta_t(N)/\delta_t(O)$, higher
 807 temperatures are retrieved, always larger than ~ 20000 K. By assuming an educated guess on
 808 decay times of $\sim 18 \mu s$ (from Kieu et al., 2019) and $\sim 140 \mu s$ (from Walker & Christian, 2019) for
 809 OI and NI respectively, we provide in Table 6 the temperature for a value $\delta_t(N)/\delta_t(O)=10$.
 810



811

812 **Figure 11** - Lightning temperature inferred from O/N atomic density ratio. Panel a): the
813 molecular dissociation model of equation (17) is shown as a black curve, while in colors are
814 represented the families of curves inferred from MAJIS data with equation (16) with different
815 ratio of temporal filling factors $\delta_t(N)/\delta_t(O)$. Red crosses indicate the solutions for the
816 temperature, given by the curves' intersections. Panel b): Families of solution for temperature
817 retrieved from MAJIS density ratios as a function of filling factor ratio.

818
819 **Table 6** - Comparison of lightning temperatures retrieved with different methods. Values in the
820 last column refer to a ratio of temporal filling factors $\delta_t(NI)/\delta_t(OI) = 10$.

flash	T (K)		
	method 1 (Sect.4.3.1)		method 2 (Sect.4.3.2)
	OI(844nm) / OI(926nm)	NI(870nm) / NI(1012nm)	OI(777nm) / NI(870nm)
A	4800 ± 1600	4000 ± 1700	23000 ± 3000
B	5400 ± 1500	4700 ± 1000	26500 ± 2500
C	5600 ± 1600	5100 ± 1200	25700 ± 2500
D	5400 ± 900	5500 ± 700	27000 ± 1500

821
822 **4.3.3. Comparison between methods**

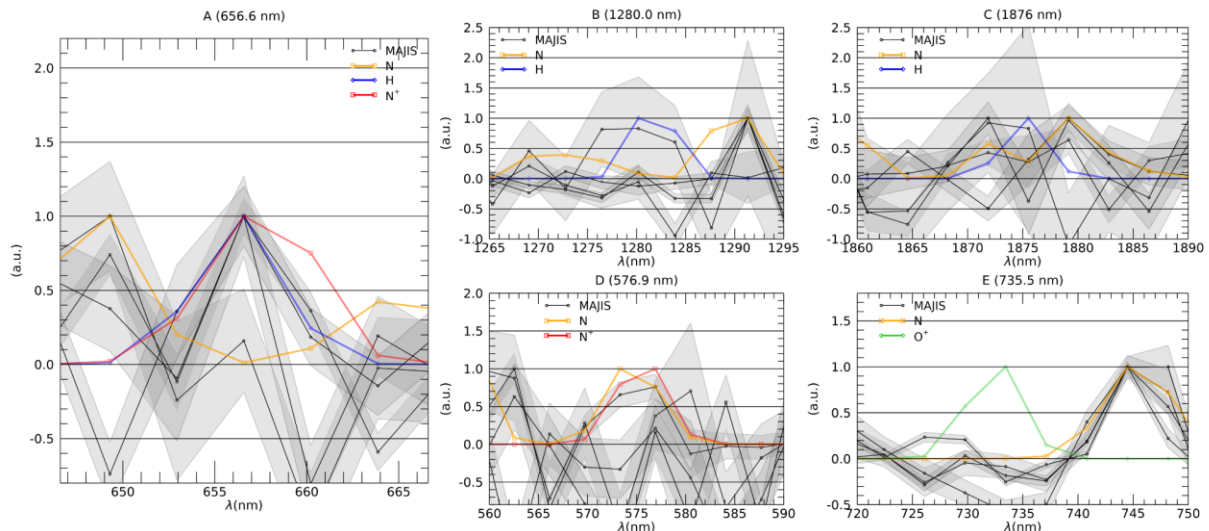
823
824 It is evident that the two methods investigated do not agree with each other on the
825 resulting lightning temperature. The ratio of temporal filling factors $\delta_{t,q}/\delta_{t,b}$ can play a key role
826 in explaining such discrepancies since its values are poorly constrained and the results are quite
827 sensitive to it. In both methods, line ratioing removes any dependence on the number of flashes
828 encompassed by a single measurement. However, lines used in method 1 (of the same species)
829 are of different intensity and are subject to the "line strength temporal bias" described in
830 Sect.3.5. Lines used in method 2 are instead of similar intensity (the strongest one for both
831 oxygen and nitrogen) but affected by uncertainty of temporal filling factors ratio. Results of
832 method 2 are somehow closer to those found in literature for peak temperatures of intra-cloud
833 lightning (see Sect.4.1), even if events generated by smaller electrical current are intrinsically
834 colder (Liu et al., 2021). Average temperatures retrieved from ground observations of cloud to
835 ground flashes are reported to lie around 17600 K, in between the results from our two methods
836 (Wemhoner et al., 2026). Actually, in order to assess which method is closer to the real
837 temperatures, we should better understand the nature of the observed event and its unresolved
838 characteristics (Sect.4.4). In any case, we can note that, as stressed in Figure 10, intra-species
839 ratios $\delta_{t,q}/\delta_{t,b}$ of the order of 3.5 (for oxygen) and 5.5 (for nitrogen) would be sufficient to
840 reconcile the results from method 1 to those of method 2.

841
842 **4.4. Signatures of other species**

844 Observations of ionized atomic emissions are often reported in the early phases of
 845 lightning processes, mainly due to N^+ , O^+ , N^{++} , O^{++} (Kieu et al., 2021). The best diagnostic
 846 features of these species fall at wavelengths shorter than those accessible by MAJIS, that might
 847 only cover their weaker lines taking place longwards of 500 nm.

848 The only significant signature present in almost all MAJIS spectra that is possibly not
 849 due to nitrogen or oxygen is found at 656.6 nm, as highlighted in Figure 12a. where the four
 850 MAJIS lightning spectra are shown in black along with their uncertainties. This wavelength
 851 encompasses the $H\alpha$ emission (656.3 nm, blue curve) which, besides being a minor component
 852 of non-LTE diffuse terrestrial exosphere emissions (e.g. Larigaldie et al., 1981), is also known
 853 to be produced in natural lightning flashes, where it can be efficiently exploited for measuring
 854 electron density (Uman & Orville, 1964). Furthermore, $H\alpha$ intensity is enhanced in wet conditions
 855 (Yingying et al., 2025), and its presence can be useful for further discriminating low-altitude
 856 discharges from upper atmosphere events. The presence of other lines of the Balmer series
 857 might make the assignment of this line to hydrogen more robust, but unfortunately $H\alpha$ is the
 858 only one falling within the MAJIS spectral range.

859 Moreover, N^+ also emits at that wavelength, with a slightly different line width (red curve).
 860 Both species have other weaker lines at longer wavelengths, N^+ at 575 nm and H at 1280 and
 861 1876 nm, that can be used for discrimination. As shown in the other panels of Figure 12, the
 862 level of noise prevents a clear detection, even if some of the MAJIS spectral shapes are slightly
 863 more correlated with H emissions rather than N^+ . Anyway, although the presence of a 656 nm
 864 peak is clear, observations are not conclusive on the nature of the emitter.



865 **Figure 12:** Comparison of MAJIS spectral shapes (frame-averaged spectra) with modeled
 866 emissions at 6000 K in selected ranges. In order to highlight possible correlations in shape, all
 867 spectra are continuum-removed and normalized to unity in the shown spectral ranges.
 868 Positive correlation only in panel A for the 656.6 nm feature with either H and N^+ emission.
 869

870
 871 A search for other small signatures has been performed without success, as in the case
 872 of O^+ shown in Figure 12E.

873 In principle, MAJIS spectra in the thermal range cover several absorption bands of NO_x
 874 molecules, whose production is known to be enhanced by lightning activity (so-called LNO_x
 875 molecules, see e.g. Schumann & Huntrieser, 2007). Opacity of thunderclouds can strongly
 876 affect the retrieval of NO_x (Beirle et al., 2019), but convection can transport NO_x released near
 877 the surface to the upper troposphere, where it is mixed with freshly produced LNO_x making

878 detection from space possible. Even if MAJIS data may offer a further chance to check the LNO_x
879 production mechanism, their absorption bands in the IR are strongly overlapped with H₂O ones,
880 and even a qualitative analysis requires a complete modeling of atmospheric thermal emission
881 which is beyond the purpose of the present work.

882

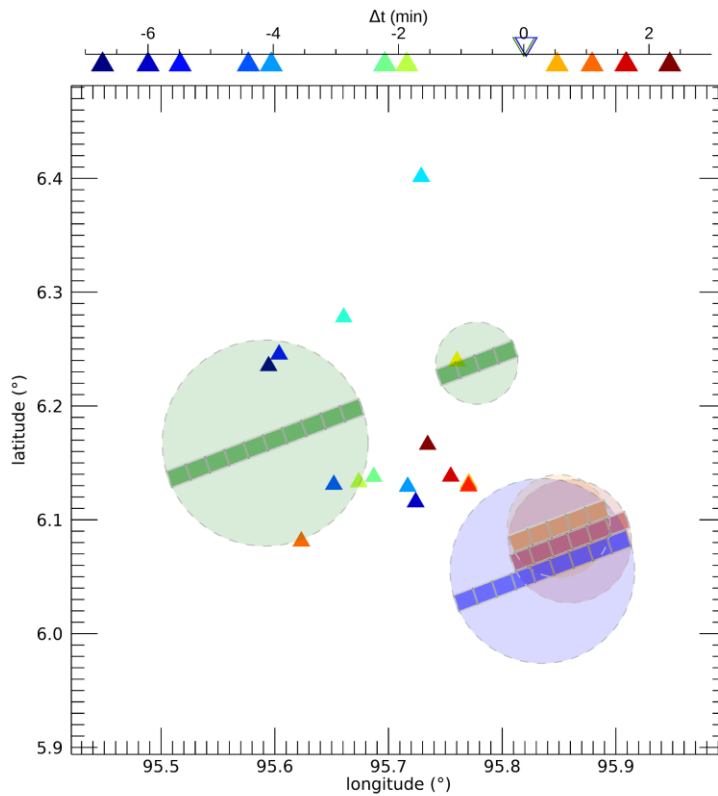
883 **4.5. Search for independent lightning detection**

884

885 We have inspected the lists of detections provided by World Wide Lightning Location
886 Network (WWLLN, Hutchins et al., 2012), the Earth Networks Total Lightning Network (ENTLN,
887 Zhu et al., 2017) and the lightning system operated by the University of Hokkaido (Narita et al.,
888 2018). As illustrated in Figure 13, a sequence of ENTLN strokes is found in the proximity of the
889 MAJIS detection, nevertheless within a few minutes before and after the MAJIS flashes,
890 indicating an active lightning area. The location of some strokes fall within the area of the first
891 MAJIS flash, but they took place ~5 min before the MAJIS observation.

892 This negative result is not surprising, as all lightning location systems mentioned above
893 are most sensitive to lightning return strokes. The return stroke lightning channels are several
894 kilometers long and thus emit the electromagnetic signals in kHz frequencies, which can travel
895 thousands of km in the waveguide formed by the surface of Earth and the bottom of the
896 ionosphere. Such signals received at several network stations are used for the localization of
897 lightning discharges by the time-of-flight method. The lightning events observed by MAJIS were
898 clearly located at the cloud tops and could be associated with high-altitude in-cloud lightning
899 phenomena as leaders, dart-leaders or streamer-like Compact Intracloud Discharges also
900 called Narrow Bipolar Events (Petersen & Beasley, 2013; Kolmašová et al., 2023b, 2026; Nag
901 et al., 2010; Liu et al., 2021; see also Rakov and Uman, 2007 for an overview on different
902 lightning phenomena). Unfortunately, the area of interest is not covered by any geostationary
903 lightning imager, which could prove a lightning activity at the cloud tops.

904 Incidentally, it is worth noting that wavy structures possibly linked to thunderstorm events
905 are observed in MAJIS images acquired during the same EGA campaign (see Oliva et al., 2025,
906 this issue) and pointing to areas adjacent to that discussed in this work, further testifying to the
907 existence of intense thunderstorm activity in the area observed by MAJIS during the EGA.



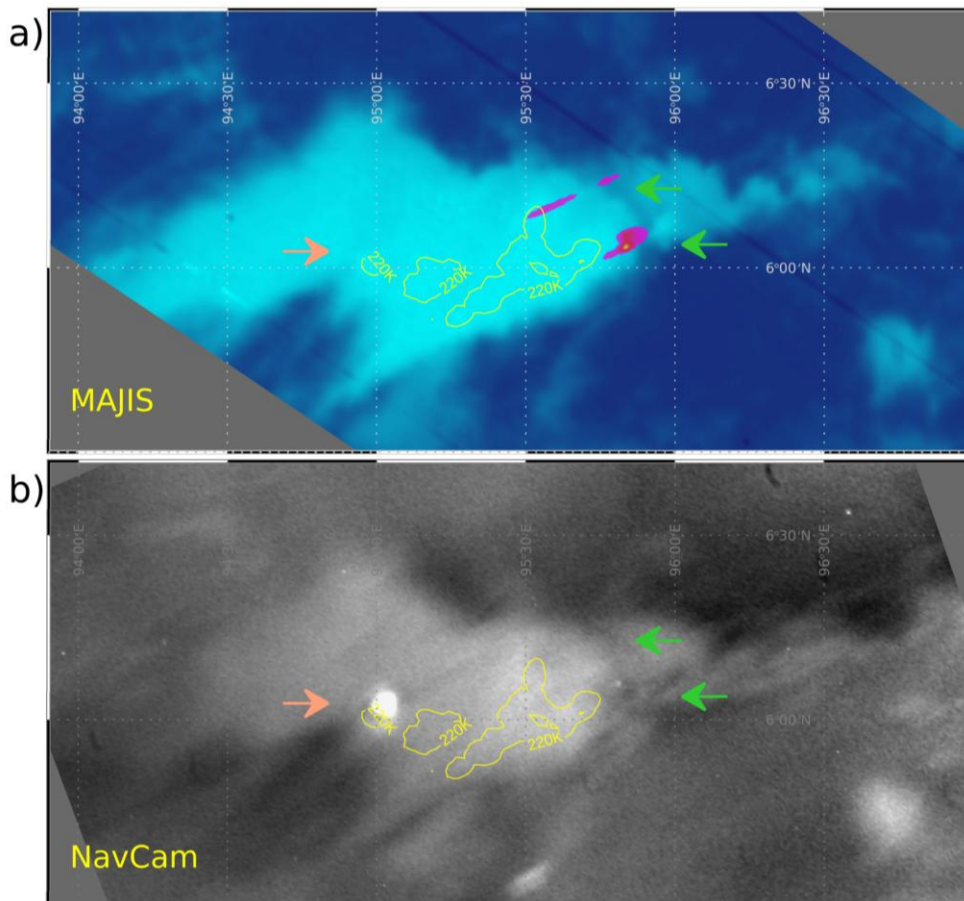
908
 909 **Figure 13:** Locations and timing of strokes detected by searched ground networks (triangles)
 910 with respect to MAJIS observations (shaded circles). Time differences of ground networks'
 911 strokes with respect to MAJIS are indicated in the upper axis.

912
 913 As accurately described in Hueso et al. (2026, this issue), lightning signatures have also
 914 been searched in the EGA dataset of JANUS (the multifilter camera of the JUICE scientific
 915 payload), without success (apart from a rather small flash, more than 2200 km far from MAJIS
 916 flashes, and probably too weak to be ascribed to lightning). JANUS acquired two images, 50 s
 917 apart, marginally covering the thunderstorm where MAJIS detects flashes (see figure 6 of Hueso
 918 et al., 2026) but, even if they are close in time to MAJIS (the second one only 2.1 s after MAJIS
 919 data), they did not cover the exact location of the MAJIS flashes, and cannot confirm their
 920 presence.

921
 922 Nevertheless, an independent confirmation of the intense lightning activity occurring in
 923 the area of interest can be found in data of the navigation camera onboard JUICE spacecraft
 924 (NavCam, Gorog et al., 2019). An image covering the same region at nearly the same time (raw
 925 image 2E57C6B857BB00, starting 2024-08-20T21:27:10.23 UTC with 2 s exposure) shows a
 926 clear detection of a lightning flash on exactly the same cloud as MAJIS, but on a different side
 927 (Figure 14). While the MAJIS flashes can be put in the clouds context through the mapping of
 928 thermal emission, in the NavCam case the flash is seen as a very intense, slightly elliptical, light
 929 blob above clouds, which are seen in reflected moonlight. At the time of writing, calibrated
 930 NavCam products are not yet available, but we took advantage of the recognizable cloud shape
 931 to spatially co-registering the NavCam image to the MAJIS one. The linear spatial resolution of
 932 the NavCam data, dominated by motion smearing, is estimated at about 2.15 km/px, and the
 933 resulting flash diameter, between 23 and 30 km, is compatible with the flashes detected by
 934 MAJIS (Table 1). The NAVCAM image has been taken about 19 s after the last MAJIS flash

935 and, on the other hand, the location of the NavCam flash (~95°E, 6°N) has been covered by
936 MAJIS about 21.5 s before NavCam. Hence no simultaneous detections were possible. Anyway,
937 this observation certainly represents a confirmation of a high flashing rate taking place in that
938 cloud.

939 The flash signal in the NavCam image is unfortunately saturated, so it cannot be used
940 for quantitative energy analysis, even in the case the calibrated data had been available.
941 Nevertheless, *Figure 14* shows that the detected flashes, in both MAJIS and NavCam cases,
942 are close to the coldest regions of the cloud, where MAJIS registered brightness temperatures
943 below 220 K, compatible with lateral light escape from areas of enhanced cloud top altitude due
944 to local convection (see Figure 4).
945



946
947 Figure 14: The same cloud observed by MAJIS (panel a) and NavCam (panel b), showing
948 lightning flashes separated by about 80 km. For helping reference, flashes' locations are
949 indicated by arrows in both panels (in orange for NavCam detection, in green for MAJIS ones).
950 Clouds contrast is provided by thermal emission in the MAJIS case (same as Figure 3) and by
951 reflected Moon-light in the NavCam case. In both panels the cloud regions with lowest MAJIS
952 brightness temperatures (<220 K) are highlighted by yellow contours. The NavCam image has
953 been taken about 19 s after the last MAJIS flash. (NavCam image credit: ESA/Juice/NavCam
954 under ESA Standard Licence).
955

956 4.6. Extrapolation to lightning detection in Jupiter's atmosphere

957
958 This serendipitous observation during the very brief Earth flyby suggests that a similar
959 opportunity could arise at Jupiter, one of the primary targets of the JUICE mission.

960 On Earth, the lightning flash rate is highly variable in space and time (e.g. Blakeslee et al., 2020).
961 The Sumatra region is one of the areas where the flash rate is higher, quantifiable during
962 summer in $\sim 30 \text{ flashes}\cdot\text{km}^{-2}\cdot\text{yr}^{-1}$ ($\sim 10^{-6} \text{ flashes}\cdot\text{km}^{-2}\cdot\text{s}^{-1}$). This made the first cube of the EGA
963 sequence the most likely to capture lightning. Taking into account the spatial and temporal
964 coverages detailed in Sect.2.1, this flash rate yields a probability of a lightning detection during
965 this cube's acquisition of $\sim 0.6\%$.

966 On Jupiter, lightning is also thought to be triggered by moist convective processes within
967 water cloud layers, at pressure levels of a few bars. Galileo spacecraft recorded good statistics
968 of optical flashes associated with lightning storms, with energy release estimated as high as
969 $\sim 10 \text{ GJ}$ (Little et al., 1999; Gierasch et al., 2000), while New Horizons spacecraft detected some
970 lightning activity at polar latitudes as well (Baines et al., 2007). These optical observations, all
971 relying on nightside imaging, suggested flash rates lower than on Earth, around 0.004
972 $\text{flashes}\cdot\text{km}^{-2}\cdot\text{yr}^{-1}$, raised to $\sim 0.07 \text{ flashes}\cdot\text{km}^{-2}\cdot\text{yr}^{-1}$ by Galileo probe dedicated analyses (Rinnert
973 et al., 1998). However, more recent observations by Juno, based on microwave measurements,
974 found on Jupiter a lightning rate comparable to Earth's one, $\sim 1\text{-}30 \text{ strokes}\cdot\text{km}^{-2}\cdot\text{yr}^{-1}$ (Kolmašová
975 et al., 2018). By considering a typical resolution of $\sim 150 \text{ km/pixel}$ and an integration time of 0.1
976 s, these latter values translate to a probability of a lightning event in a single MAJIS pixel at
977 Jupiter around $0.07\text{-}1\%$. If the discrepancy in flash rate between optical and microwave
978 observations is not sample-biased but is due to different atmospheric opacity, then the lower
979 flash rates have to be assumed for MAJIS, lowering the detection probability per pixel to 10^{-6} .
980 From the spectral point of view, since the composition of the Jovian atmosphere is very different
981 from that of Earth, a possible detection of lightning should rely on totally different spectral
982 signatures. To estimate the most likely emission lines detectable by MAJIS, we considered a
983 unique gaseous layer with a standard Jovian atmosphere composition (populated by H_2 , He,
984 H_2O , CH_4 , NH_3 , Ne, H_2S , Ar, Kr, Xe, with fixed mixing ratios 0.84 , 0.16 , $1.5\text{e-}3$, $1.8\text{e-}4$, $1.9\text{e-}4$,
985 $3.1\text{e-}5$, $6.1\text{e-}6$, $1.5\text{e-}9$, $7\text{e-}11$ respectively), then we evaluated the abundances of their
986 dissociation products by using the simplified model of equation (17). Dissociation energies are
987 set to the following values: $D(\text{O}_2)=498 \text{ kJ/mol}$, $D(\text{H}_2)=431 \text{ kJ/mol}$, $D(\text{CH}_4\rightarrow\text{H}+\text{CH}_3)=463.1$
988 kJ/mol , $D(\text{CH}_3\rightarrow\text{CH}_2+\text{H})=463.1 \text{ kJ/mol}$, $D(\text{CH}_2\rightarrow\text{CH}+\text{H})=422.6 \text{ kJ/mol}$, $D(\text{CH}\rightarrow\text{C}+\text{H})=338.7$
989 kJ/mol , $D(\text{H}_2\text{O})=497.3 \text{ kJ/mol}$ (Ruscic, 2015), $D(\text{NH}_3\rightarrow\text{NH}_2+\text{H})=3226 \text{ cm}^{-1}$ (McCarthy et al.,
990 1987), $D(\text{H}_2\text{S}\rightarrow\text{H}_2+\text{S})=0.2 \text{ eV/mol}$ (Gutsol et al., 2010). Finally the ratios of atomic abundances
991 are used to estimate the relative intensities of potential lightning emission. Results of the
992 calculation are shown in Table 7, for a lightning temperature of 1000 K .
993 It is not surprising that hydrogen would dominate Jovian lightning spectra, being by far the most
994 abundant species. The strongest line is the $\text{H}\alpha$, but several other hydrogen lines could reach a
995 significant intensity. Most of the lightning energy ($> 60\%$ of the total) should escape through the
996 $649\text{-}660 \text{ nm}$ wavelength range, but a significant energy flux ($\sim 30\%$) may occur through the
997 $1871\text{-}1879 \text{ nm}$ window. Secondary but still possibly relevant ranges are $1280\text{-}1284 \text{ nm}$ and
998 $1090\text{-}1094 \text{ nm}$ ($\sim 5\%$ and $\sim 1\%$ of the total energy respectively).
999 The only other species reaching a comparable level of intensity within the MAJIS spectral range
1000 is sulphur, whose line at 922.3 nm could reach 1% intensity of the $\text{H}\alpha$. All other atomic species
1001 are confined at lower intensities, starting from the oxygen line at 777 nm expected to reach a
1002 0.08% level.

1003 For a more comprehensive simulation of the MAJIS signal from Jovian lightning, both
1004 instrumental response and scattering/absorbing spectral properties of overlying cloud layers
1005 have to be taken into account. For instance, the instrumental NESR derived by background
1006 fluctuations (see Figure 2b) can be slightly larger near 650 nm than near 1870 nm , partially
1007 compensating the relative detection probability mentioned above. On the other hand, emission

1008 lines located inside strong methane absorption bands may have an enhanced detection
 1009 probability due to reduced scattered light, increasing their visibility on the planet's dayside as
 1010 well, as recently reported by JunoCam analyses (Fletcher et al., 2026). The full setting of
 1011 instrumental parameters will be also crucial for optimizing both the probability of detection and
 1012 interpretation of lightning events, and will be better assessed in future planning. Also, a
 1013 quantitative estimation of SNR requirements, that would require more complex models to
 1014 calculate the absolute abundances of potential emitters, is beyond the purpose of this work.

1015 In case of detection, lightning temperature retrievals in Jupiter's case should rely solely
 1016 on method 1 (Sect.4.2.1), being signatures of species other than hydrogen unlikely. In this
 1017 context, the coverage of both 650 nm and 1870 nm spectral ranges is effective for constraining
 1018 temperature, as they probe a suitable variety of electronic level populations. However, issues
 1019 related to spatially and temporally unresolved measurements will hold also in the jovian case,
 1020 and a more accurate de-biasing, based on detailed models of atmospheric and instrumental
 1021 processes, will be desirable.

1022
 1023 **Table 7-** Modeled ratios of line intensities for lightning emissions in Jupiter's atmosphere,
 1024 relative to the H α line, for a lightning temperature of 1000 K.

multiplet	line ratio	multiplet	line ratio	multiplet	line ratio
H α (656.6 nm)	100%	H (1879.2 nm)	7%	H (1944.8 nm)	1%
H (1875.5 nm)	57%	H (1283.9 nm)	6%	H (1004.3 nm)	1%
H (652.9 nm)	36%	H (1093.9 nm)	4%	H (1090.2 nm)	1%
H (660.2 nm)	24%	H (2164.6 nm)	1%	H (1997.6 nm)	1%
H (1871.9 nm)	14%	H (649.3 nm)	1%	S (922.3 nm)	0.74%
H (1280.2 nm)	8%	H (2168.3 nm)	1%	O (777.7 nm)	0.08%

1025
 1026 **5. Summary and conclusion**

1027
 1028 The data acquired by MAJIS during the JUICE Earth Gravity Assist maneuver on 2024,
 1029 Aug, 20th, revealed a serendipitous detection of lightning emissions, taking place at nighttime
 1030 near Sumatra island. The detection consists of a few spectra in the visible range showing
 1031 emission lines diagnostic of neutral atomic oxygen and nitrogen. Oxygen is clearly identified by
 1032 the 777 nm line, routinely used in monitoring lightning activity by satellite, whereas nitrogen
 1033 strongest emissions take place at 870 nm and 822 nm. An emission is also found at 656.6 nm,
 1034 even though we cannot conclusively discriminate between contributions by H or N⁺. The
 1035 observed four flashes can be localized near the edge of a thick thunderstorm cloud, but we did
 1036 not find any independent detection of the same events neither by ground-based lightning
 1037 networks nor by satellites.

1038 Although the characteristics of MAJIS observations are not optimal for measuring such
 1039 extreme phenomena, we attempt to model the MAJIS emission spectra in order to retrieve as
 1040 much physical information as possible. In particular, MAJIS could not resolve the lightning flash
 1041 features neither spectrally nor temporally, raising the need for specific corrections to the
 1042 standard calibrated spectral radiance values, quantified where possible through spectral and
 1043 temporal filling factors. Under these assumptions, we estimate the flashes emitted through the

1044 777 nm oxygen line an energy of 140-700 kJ, and up to 1.3 MJ for the event considered as a
1045 whole.

1046 The relative intensity of emission lines is a well-known proxy for measuring the
1047 temperature of the lightning channel. We attempt to apply this method to both ratios of oxygen
1048 lines and nitrogen lines, but the obtained temperatures, ranging between 4000 and 5600 K, with
1049 uncertainties of the order of 30%, appear well below the peak temperatures of intra-cloud
1050 lightning reported in literature (20000-35000 K), but compatible with colder phenomena like
1051 streamer-like discharges and narrow bipolar events (Liu et al., 2021).

1052 An alternative approach for temperature retrieval from ratios of oxygen to nitrogen lines
1053 has also been attempted. In this case much higher values are retrieved, around 23000-27000
1054 K, closer to the highest peak temperature values. Both methods can yield temperatures biased
1055 by our incomplete knowledge of the temporal trend of individual lines within the lightning flashes.
1056 A more robust assessment in this regard is not possible without independent knowledge of the
1057 nature and unresolved characteristics of the event, since the MAJIS observation could have
1058 registered different types of transient luminous events occurring in short times at different
1059 temperatures.

1060 The EGA data here discussed represent the first ones acquired by MAJIS on a planetary
1061 target. From this point of view, the analysis demonstrates the valuable performances of the
1062 instrument also on an unexpected finding. This is also true in the case of Jupiter's atmosphere,
1063 a primary target of the JUICE mission. Considering also that Jupiter's atmosphere is thought to
1064 host a high-energy lightning rate as high as on Earth (Kolmašová et al., 2018, Wong et al.,
1065 2026), repeated MAJIS observations of the Jovian night hemisphere have a non-zero chance
1066 to capture lightning flash spectra. Hence, this work is also intended to help planning and analysis
1067 of future Jupiter observations. In that case, several synergistic approaches with other JUICE
1068 instruments can be envisaged, like UVS for detecting shorter-wavelength emission lines,
1069 JANUS for higher spatial resolution context images, or RPWI for coincident radio signals. Even
1070 if the likelihood of simultaneous observations of the same event will decrease proportionally to
1071 the number of observing constraints to be satisfied, a comparison of events on a statistical basis
1072 at global scale could be achieved.

1073
1074 **Code availability** - Simple scripts have been developed for data management and processing
1075 and for the implementation of the models described to MAJIS data. The codes will not be
1076 published but can be shared upon private request to the corresponding author.

1077
1078 **Data availability** - The MAJIS data acquired during the JUICE Moon–Earth flyby in August 2024
1079 are currently under the mission's cruise-phase proprietary period. These data will be made
1080 available through the ESA Planetary Science Archive following the first Cruise Archive Delivery,
1081 which is currently scheduled for six months after Earth Gravity Assist #3 in 2029.

1082
1083 **Author contribution** - ED carried out lightning data identification and processing, ED and FO
1084 developed data analysis, interpretation, and manuscript preparation, with significant
1085 contributions by FP, GP, AM, LF, BS. IK performed ground-based lightning counterparts search,
1086 BS provided NavCam flash detection, while FP, GP, YL, GF, SR, BS provided calibrated MAJIS
1087 data. All coauthors contributed to the discussion of results.

1088
1089 **Competing interests** - The authors declare that they have no conflict of interest.

1090
1091 **Acknowledgments**

1092
1093 The authors want to thank Thomas Cornet and the whole team at ESA Science
1094 Operation Centre for providing NavCam data and managing Juice mission operations.
1095 JUICE is a mission under ESA leadership with contributions from its Member States,
1096 NASA, JAXA and the Israel Space Agency. It is the first Large-class mission in ESA's Cosmic
1097 Vision programme. NavCam instrument has been provided through an ESA Contract with
1098 Airbus.
1099 The Italian participation in the JUICE mission is funded by the Italian Space Agency
1100 (ASI). In particular, this work has been developed under the ASI-INAF agreement n. 2023-6-
1101 HH.0.

1102 1103 **References**

- 1104
1105 Acton, C. H. Jr.: Ancillary data services of NASA's Navigation and Ancillary Information
1106 Facility, *Planet. Space Sci.*, 44(1), 65–70, [https://doi.org/10.1016/0032-](https://doi.org/10.1016/0032-0633(95)00107-7)
1107 [0633\(95\)00107-7](https://doi.org/10.1016/0032-0633(95)00107-7), 1996.
1108 Acton, C., Bachman, N., Semenov, B., and Wright, E.: A look towards the future in the
1109 handling of space science mission geometry, *Planet. Space Sci.*, 150, 9–12,
1110 <https://doi.org/10.1016/j.pss.2017.02.013>, 2018.
1111 Aplin, K. L., and Fischer, G.: Lightning detection in planetary atmospheres, *Weather*, 72(2),
1112 46–50, <https://doi.org/10.1002/wea.2817>, 2017.
1113 Bai, X., Füllekrug, M., Chanrion, O., Soula, S., Peverell, A., Mashao, D., Kosch, M., Husbjerg,
1114 L., Østgaard, N., Neubert, T., and Reglero, V.: Height determination of a blue
1115 discharge observed by ASIM/MMIA on the International Space Station, *J. Geophys.*
1116 *Res. D: Atmospheres*, e2022JD037460, <https://doi.org/10.1029/2022jd037460>, 2023.
1117 Barnes, D. E., Splitt, M. E., Dwyer, J. R., Lazarus, S., Smith, D. M., & Rassoul, H. K.: A study
1118 of thunderstorm microphysical properties and lightning flash counts associated with
1119 terrestrial gamma-ray flashes, *J. Geophys. Res. D: Atmospheres*, 120(8), 3453–3464.
1120 <https://doi.org/10.1002/2014jd021495>, 2015.
1121 Barvir, P., Kubes, P., Krawarik, J., Scholz, M., Karpinski, L., Sadowska-Skladnik, E., &
1122 Malinowski, K.: Research of the discharge with parameters of lightning channel,
1123 *Czechoslovak Journal of Physics*, 54(S3), C274–C278.
1124 <https://doi.org/10.1007/bf03166412>, 2004.
1125 Becker, H. N., Alexander, J. W., Atreya, S. K., Bolton, S. J., Brennan, M. J., Brown, S. T.,
1126 Guillaume, A., Guillot, T., Ingersoll, A. P., Levin, S. M., Lunine, J. I., Aglyamov, Y. S., &
1127 Steffes, P. G.: Small lightning flashes from shallow electrical storms on Jupiter, *Nature*,
1128 584(7819), 55–58, <https://doi.org/10.1038/s41586-020-2532-1>, 2020.
1129 Beirle, S., Borger, C., Dörner, S., Li, A., Hu, Z., Liu, F., Wang, Y., & Wagner, T.: Pinpointing
1130 nitrogen oxide emissions from space, *Sci. Adv.*, 5, eaax9800,
1131 <https://doi.org/10.1126/sciadv.aax9800>, 2019.
1132 Bjørge-Engeland, I., Østgaard, N., Marisaldi, M., Luque, A., Mezentsev, A., Lehtinen, N.,
1133 Chanrion, O., Fuglestad, A. N., Neubert, T., & Gordillo-Vazquez, F. J.: High peak
1134 current lightning and the production of elves. *J. Geophys. Res. D: Atmospheres*,
1135 129(4), <https://doi.org/10.1029/2023jd039849>, 2024.
1136 Blakeslee, R. J., Lang, T. J., Koshak, W. J., Buechler, D., Gatlin, P., Mach, D. M., Stano, G.
1137 T., Virts, K. S., Walker, T. D., Cecil, D. J., Ellett, W., Goodman, S. J., Harrison, S.,
1138 Hawkins, D. L., Heumesser, M., Lin, H., Maskey, M., Schultz, C. J., Stewart, M.,
1139 Bateman, M., Chanrion, O., Christian, H.: Three years of the lightning imaging sensor
1140 onboard the international space station: Expanded global coverage and enhanced
1141 applications, *J. Geophys. Res. D: Atmospheres*, 125(16),
1142 <https://doi.org/10.1029/2020jd032918>, 2020.
1143 Boccippio, D. J., Cummins, K. L., Christian, H. J., & Goodman, S. J.: Combined satellite- and
1144 surface-based estimation of the intracloud–cloud-to-ground lightning ratio over the

1145 continental United States, *Mon. Wea. Rev.*, 129, 108–122,
1146 [https://doi.org/10.1175/1520-0493\(2001\)129<0108:csasbe>2.0.co;2](https://doi.org/10.1175/1520-0493(2001)129<0108:csasbe>2.0.co;2), 2001.

1147 Boggs, L. D., Liu, N., Nag, A., Walker, T. D., Christian, H. J., da Silva, C. L., Austin, M.,
1148 Aguirre, F., & Rassoul, H. K.: Vertical temperature profile of natural lightning return
1149 strokes derived from optical spectra, *J. Geophys. Res. D: Atmospheres*, 126(8),
1150 e2020JD034438, <https://doi.org/10.1029/2020jd034438>, 2021.

1151 Brown, S., Janssen, M., Adumitroaie, V., Atreya, S., Bolton, S., Gulkis, S., Ingersoll, A., Levin,
1152 S., Li, C., Li, L., Lunine, J., Misra, S., Orton, G., Steffes, P., Tabataba-Vakili, F.,
1153 Kolmašová, I., Imai, M., Santolík, O., Kurth, W., Hospodarsky, G., Gurnett, D.,
1154 Connerney, J.: Prevalent lightning sferics at 600 megahertz near Jupiter's poles,
1155 *Nature*, 558(7708), 87–90. <https://doi.org/10.1038/s41586-018-0156-5>, 2018.

1156 Cardesín Moinelo, A., Abildgaard, S., García Muñoz, A., Piccioni, G., & Grassi, D.: No
1157 statistical evidence of lightning in Venus night-side atmosphere from VIRTIS-Venus
1158 Express Visible observations, *Icarus*, 277, 395–400,
1159 <https://doi.org/10.1016/j.icarus.2016.05.027>, 2016.

1160 Carvalho, F. L., Uman, M. A., Jordan, D. M., Wilkes, R. A., & Kotovsky, D. A.: Triggered
1161 lightning return stroke luminosity up to 1 km in two optical bands, *J. Geophys. Res. D:*
1162 *Atmospheres*, 123(17), 9724–9740, <https://doi.org/10.1029/2018jd028644>, 2018.

1163 Cecil, D. J., Buechler, D. E., & Blakeslee, R. J.: Gridded lightning climatology from TRMM-LIS
1164 and OTD: Dataset description, *Atmos. Res.*, 135–136, 404–414,
1165 <https://doi.org/10.1016/j.atmosres.2012.06.028>, 2014.

1166 Christian, H. J., Blakeslee, R. J., Boccippio, D. J., Boeck, W. L., Buechler, D. E., Driscoll, K.
1167 T., Goodman, S. J., Hall, J. M., Koshak, W. J., Mach, D. M., & Stewart, M. F.: Global
1168 frequency and distribution of lightning as observed from space by the Optical Transient
1169 Detector, *J. Geophys. Res. D: Atmospheres*, 108(D1).
1170 <https://doi.org/10.1029/2002jd002347>, 2003.

1171 Christian, H. J., & Goodman, S. J.: Optical observations of lightning from a high-altitude
1172 airplane, *J. Atmos. Oceanic Technol.*, 4(4), 701–711, [https://doi.org/10.1175/1520-0426\(1987\)004<0701:ooofa>2.0.co;2](https://doi.org/10.1175/1520-0426(1987)004<0701:ooofa>2.0.co;2), 1987.

1174 Cox, Arthur N., ed. (2002). "11. Earth". *Allen's Astrophysical Quantities* (4th ed.). New York,
1175 NY: Springer New York. doi:10.1007/978-1-4612-1186-0. ISBN 978-1-4612-7037-9.

1176 Darwent, B. deB. Bond Dissociation Energies in Simple Molecules. U.S. National Bureau of
1177 Standards, NSRDS-NBS 31, Washington, DC, LCCN 70602101.
1178 <https://lccn.loc.gov/70602101>. 1970.

1179 Dyudina, U., Delgenio, A., Ingersoll, A., Porco, C., West, R., Vasavada, A., & Barbara, J.:
1180 Lightning on Jupiter observed in the line by the Cassini imaging science subsystem,
1181 *Icarus*, 172(1), 24–36, <https://doi.org/10.1016/j.icarus.2004.07.014>, 2004.

1182 Filacchione, G., Haffoud, P., Poulet, F., Piccioni, G., Langevin, Y., Tommasi, L., Barbis, A.,
1183 Carter, J., Guerri, I., Dumesnil, C., De Angelis, S., Vincendon, M., Stefani, S., Pilorget,
1184 C., Tosi, F., & Rodriguez, S.: Calibration of MAJIS (Moons And Jupiter Imaging
1185 Spectrometer). II. Spatial calibration, *Rev. Sci. Instrum.*, 95(4), 041301,
1186 <https://doi.org/10.1063/5.0203872>, 2024.

1187 Fischer, G., Desch, M., Zarka, P., Kaiser, M., Gurnett, D., Kurth, W., MacHer, W., Rucker, H.,
1188 Lecacheux, A., & Farrell, W.: Saturn lightning recorded by Cassini/RPWS in 2004,
1189 *Icarus*, 183(1), 135–152, <https://doi.org/10.1016/j.icarus.2006.02.010>, 2006.

1190 Fletcher, L. N., Zhang, Z., Brown, S., Oyafuso, F. A., Rogers, J. H., Wong, M. H., et al. (2026).
1191 Structure of Jupiter's high-latitude storms: Folded filamentary regions revealed by
1192 Juno. *Journal of Geophysical Research: Planets*, 131, e2025JE009315.
1193 <https://doi.org/10.1029/2025JE009315>, 2026.

1194 Franzblau, E., & Popp, C. J.: Nitrogen oxides produced from lightning. *Journal of Geophysical*
1195 *Research: Atmospheres*, 94(D8), 11089–11104,
1196 <https://doi.org/10.1029/jd094id08p11089>, 1989.

1197 Frost, D.C., & McDowell, C. A.: The dissociation energy of the nitrogen molecule. *Proc. A*, 236
1198 (1205), 278–284. <https://doi.org/10.1098/rspa.1956.0135>, 1956.

1199 Giles, R. S., Greathouse, T. K., Bonfond, B., Gladstone, G. R., Kammer, J. A., Hue, V.,

- 1200 Grodent, D. C., Gérard, J., Versteeg, M. H., Wong, M. H., Bolton, S. J., Connerney, J.
 1201 E. P., & Levin, S. M.: Possible transient luminous events observed in Jupiter's upper
 1202 atmosphere, *J. Geophys. Res. E: Planets*, 125(11), e2020JE006659,
 1203 <https://doi.org/10.1029/2020je006659>, 2020.
- 1204 Gjesteland, T., Østgaard, N., Bitzer, P., & Christian, H. J.: On the timing between terrestrial
 1205 gamma ray flashes, radio atmospheric, and optical lightning emission, *J. Geophys.*
 1206 *Res. A: Space Physics*, 122(7), 7734–7741, <https://doi.org/10.1002/2017ja024285>,
 1207 2017.
- 1208 Goodman, S. J., Blakeslee, R. J., Koshak, W. J., Mach, D., Bailey, J., Buechler, D., Carey, L.,
 1209 Schultz, C., Bateman, M., McCaul, E., Jr., & Stano, G.: The GOES-R Geostationary
 1210 Lightning Mapper (GLM), *Atmos. Res.*, 125–126, 34–49,
 1211 <https://doi.org/10.1016/j.atmosres.2013.01.006>, 2013.
- 1212 Gordillo-Vázquez, F. J., & Pérez-Invernón, F. J.: A review of the impact of transient luminous
 1213 events on the atmospheric chemistry: Past, present, and future, *Atmos. Res.*, 252,
 1214 105432. <https://doi.org/10.1016/j.atmosres.2020.105432>, 2021.
- 1215 Gorog, F., M.-C. Arnolfo, S. Belmana, S. Dervaux, D. Gherardi: JUICE navigation camera
 1216 design, *Proc. SPIE 11180, International Conference on Space Optics — ICSO 2018*,
 1217 111804N (12 July 2019); <https://doi.org/10.1117/12.2536086>, 2019.
- 1218 Gosse, L., Favre, A., Bultel, A., Morel, V., Djurović, S., Simić, N., & Gavanski, L.: In-depth
 1219 Stark broadening study of neutral oxygen 777 nm triplet, *Spectrochim. Acta Part B:*
 1220 *Atomic Spectroscopy*, 230, 107222. <https://doi.org/10.1016/j.sab.2025.107222>, 2025.
- 1221 Gurnett, D. A., Kurth, W. S., Cairns, I. H., & Granroth, L. J.: Whistlers in Neptune's
 1222 magnetosphere: Evidence of atmospheric lightning, *J. Geophys. Res. A: Space*
 1223 *Physics*, 95(A12), 20967–20976, <https://doi.org/10.1029/ja095ia12p20967>, 1990.
- 1224 Gurnett, D. A., Shaw, R. R., Anderson, R. R., Kurth, W. S., & Scarf, F. L.: Whistlers observed
 1225 by Voyager 1: Detection of lightning on Jupiter, *Geophys. Res. Lett.*, 6(6), 511–514.
 1226 <https://doi.org/10.1029/gi006i006p00511>, 1979.
- 1227 Gutsol, K., Nunnally, T., Rabinovich, A., Fridman, A., Starikovskiy, A., Gutsol, A., & Potter, R.
 1228 W.: Mechanisms of non-equilibrium dissociation of hydrogen sulfide in low-temperature
 1229 plasma, 2010 Abstracts IEEE International Conference on Plasma Science, Norfolk,
 1230 VA, USA, 2010, pp. 1-1, <https://doi.org/10.1109/plasma.2010.5534017>, 2010.
- 1231 Haffoud, P., Poulet, F., Vincendon, M., Filacchione, G., Barbis, A., Guiot, P., Lecomte, B.,
 1232 Langevin, Y., Piccioni, G., Dumesnil, C., Rodriguez, S., Carter, J., Stefania, S.,
 1233 Tommasi, L., Tosi, F., & Pilorget, C.: Calibration of MAJIS (Moons And Jupiter Imaging
 1234 Spectrometer). III. Spectral calibration, *Rev. Sci. Instrum.*, 95(3),
 1235 <https://doi.org/10.1063/5.0188944>, 2024.
- 1236 Hueso, R., Antuñano, A., Lara, L. M., Stephan, K., Zinzi, A., Coustenis, A., Yair, Y., Sato, M.,
 1237 Haruyama, J., Simon, A., Tubiana, C., Penasa, L., Agostini, L., Luchetti, A., Aboudan,
 1238 A., Aye, M., Kersten, E., Matz, K.-D., Politti, R., Trauthan, F., Evill, R., Belgacem, I.,
 1239 Yukihiro, T., Castro-Marín, J. M., Della Corte, V., Hviid, S., Roatsch, T., Schmitz, N.,
 1240 Patel, M., Portyankina, G., and Palumbo, P.: JUICE-JANUS observations of Earth in
 1241 preparation for the JANUS investigation of Jupiter's atmosphere, *EGUsphere*
 1242 [preprint], <https://doi.org/10.5194/egusphere-2026-710>, 2026.
- 1243 Hutchins, M. L., Holzworth, R. H., Rodger, C. J., & Brundell, J. B.: Far-field power of lightning
 1244 strokes as measured by the World Wide Lightning Location Network, *J. Atmos.*
 1245 *Oceanic Technol.*, 29(8), 1102–1110, <https://doi.org/10.1175/jtech-d-11-00174.1>, 2012.
- 1246 Ivenko, I. B., Parnikov, S. G., & Alekseev, V. N.: Variations of the Nightglow 557.7 nm
 1247 Emission Intensity during Solar Cycle 23, *Geomag. Aeron.*, 59(6), 738–742,
 1248 <https://doi.org/10.1134/s0016793219050050>, 2019.
- 1249 Imai, M., Kolmašová, I., Kurth, W. S., Santolík, O., Hospodarsky, G. B., Gurnett, D. A., Brown,
 1250 S. T., Bolton, S. J., Connerney, J. E. P., & Levin, S. M.: Evidence for low density holes
 1251 in Jupiter's ionosphere. *Nat. Commun.*, 10(1), <https://doi.org/10.1038/s41467-019-10708-w>, 2019.
- 1253 Jadhav, D. B., Londhe, A. L., & Bose, S.: Observations of NO₂ and O₃ during thunderstorm
 1254 activity using visible spectroscopy, *Adv. Atmos. Sci.*, 13(3), 359–374.

1255 <https://doi.org/10.1007/bf02656853>, 1996.

1256 Joule, J. P.: Spectrum of lightning. *Nature*, 6(139), 161, <https://doi.org/10.1038/006161b0>,

1257 1872.

1258 ESA SPICE Service: JUICE Operational SPICE Kernel Dataset, [https://doi.org/10.5270/esa-](https://doi.org/10.5270/esa-ybmj68p)

1259 [ybmj68p](https://doi.org/10.5270/esa-ybmj68p), 2019.

1260 Kieu, N., Gordillo-Vázquez, F. J., Passas, M., Sánchez, J., Pérez-Invernón, F. J., Luque, A.,

1261 Montanyá, J., & Christian, H.: Submicrosecond spectroscopy of lightning-like

1262 discharges: Exploring new time regimes, *Geophys. Res. Lett.*, 47(15),

1263 <https://doi.org/10.1029/2020gl088755>, 2020.

1264 Kieu, N., Gordillo-Vázquez, F. J., Passas, M., Sánchez, J., & Pérez-Invernón, F. J.: High-

1265 speed spectroscopy of lightning-like discharges: Evidence of molecular optical

1266 emissions, *J. Geophys. Res. D: Atmospheres*, 126(11).

1267 <https://doi.org/10.1029/2021jd035016>, 2021.

1268 Köhn, C., Heumesser, M., Chanrion, O., Reglero, V., Østgaard, N., Christian, H. J., Lang, T.

1269 J., Blakeslee, R. J., & Neubert, T.: Employing optical lightning data to identify lightning

1270 flashes associated to terrestrial gamma-ray flashes, *Bull. Atmos. Sci. Technol.*, 5(1),

1271 <https://doi.org/10.1007/s42865-024-00065-y>, 2024.

1272 Kolmašová, I., Imai, M., Santolík, O., Kurth, W. S., Hospodarsky, G. B., Gurnett, D. A.,

1273 Connerney, J. E. P., & Bolton, S. J.: Discovery of rapid whistlers close to Jupiter

1274 implying lightning rates similar to those on Earth, *Nat. Astron.*, 2(7), 544–548,

1275 <https://doi.org/10.1038/s41550-018-0442-z>, 2018.

1276 Kolmašová, I., Santolík, O., Imai, M., Kurth, W. S., Hospodarsky, G. B., Connerney, J. E. P.,

1277 Bolton, S. J., & Lán, R.: Lightning at Jupiter pulsates with a similar rhythm as in-cloud

1278 lightning at Earth, *Nat. Commun.*, 14(1), <https://doi.org/10.1038/s41467-023-38351-6>,

1279 2023a.

1280 Kolmašová, I., Scholten, O., Santolík, O., Hare, B. M., Zacharov, P., Lán, R., et al.: A strong

1281 pulsing nature of negative intracloud dart leaders accompanied by regular trains of

1282 microsecond-scale pulses. *Geophysical Research Letters*, 50, e2023GL103864.

1283 <https://doi.org/10.1029/2023GL103864>, 2023b.

1284 Kolmašová, I., Soula, S., Santolík, O., Defer, E., Zhu, Y., Pédeboy, S., et al.: Properties of

1285 positive narrow bipolar events observed in South-Eastern France. *Journal of*

1286 *Geophysical Research: Atmospheres*, 131, e2025JD045415.

1287 <https://doi.org/10.1029/2025JD045415>, 2026.

1288 Kramida, A., Ralchenko, Yu., Reader, J. and NIST ASD Team: NIST Atomic Spectra

1289 Database (version 5.12), online available: <https://physics.nist.gov/asd> [Mon Dec 29

1290 2025], National Institute of Standards and Technology, Gaithersburg, MD,

1291 <https://doi.org/10.18434/T4W30F>, 2024.

1292 Kramida, A.: Evaluation of uncertainties in atomic data on spectral lines and transition

1293 probabilities. *Eur. Phys. J. D* 78, 36, <https://doi.org/10.1140/epjd/s10053-024-00820-y>,

1294 2024.

1295 Krider, E. P.: Time-resolved spectral emissions from individual return strokes in lightning

1296 discharges, *J. Geophys. Res.*, 70(10), 2459–2460,

1297 <https://doi.org/10.1029/jz070i010p02459>, 1965.

1298 Krider, E.P.: Lightning spectroscopy, *Nuclear Instruments and Methods*, 110, 411–419,

1299 [https://doi.org/10.1016/0029-554x\(73\)90720-9](https://doi.org/10.1016/0029-554x(73)90720-9), 1973.

1300 Langevin, Y., Zambelli, M., Guiot, P.: On-board de-spiking implemented by MAJIS, the

1301 VIS/NIR imaging spectrometer of JUICE, *Proc. SPIE* 11443, *Space Telescopes and*

1302 *Instrumentation 2020: Optical, Infrared, and Millimeter Wave*, 1144378,

1303 <https://doi.org/10.1117/12.2562464>, 2020.

1304 Langevin, Y., Poulet, F., Piccioni, G., Filacchione, G., Dumesnil, C., Tosi, F., Carter, J., Barbis,

1305 A., Haffoud, P., Tommasi, L., Vincendon, M., De Angelis, S., Guerri, I., Pilorget, C.,

1306 Rodriguez, S., Stefani, S., Bolsée, D., Cisneros, M., Van Laeken, L., Pereira, N.,

1307 Carapelle, A.: Calibration of MAJIS (Moons and Jupiter Imaging Spectrometer). IV.

1308 Radiometric calibration (invited). *Rev. Sci.Instrum.*, 95(11).

1309 <https://doi.org/10.1063/5.0202702>, 2024.

- 1310 Langford, A. O., Portmann, R. W., Daniel, J. S., Miller, H. L., & Solomon, S.: Spectroscopic
1311 measurements of NO₂ in a Colorado thunderstorm: Determination of the mean
1312 production by cloud-to-ground lightning flashes, *J. Geophys. Res. D: Atmospheres*,
1313 109(D11), <https://doi.org/10.1029/2003jd004158>, 2004.
- 1314 Larigaldie, S., Labaune, G., & Moreau, J. P.: Lightning leader laboratory simulation by means
1315 of rectilinear surface discharges, *J. Appl. Phys.*, 52(12), 7114–7120,
1316 <https://doi.org/10.1063/1.328420>, 1981.
- 1317 Li, D., Luque, A., Gordillo-Vázquez, F. J., Liu, F., Lu, G., Neubert, T., Chanrion, O., Zhu, B.,
1318 Østgaard, N., & Reglero, V.: Blue flashes as counterparts to narrow bipolar events: the
1319 optical signal of shallow in-cloud discharges, *J. Geophys. Res.: Atmospheres*, 126(13),
1320 <https://doi.org/10.1029/2021jd035013>, 2021.
- 1321 Li, X., Zhang, J., Chen, L., Xue, Q., & Zhu, R.: Measuring method for lightning channel
1322 temperature. *Sci. Rep.*, 6(1), <https://doi.org/10.1038/srep33906>, 2016.
- 1323 Liu, F., Lu, G., Neubert, T., Lei, J., Chanrion, O., Østgaard, N., Li, D., Luque, A., Gordillo-
1324 Vázquez, F. J., Reglero, V., Lyu, W., & Zhu, B.: Optical emissions associated with
1325 narrow bipolar events from thunderstorm clouds penetrating into the stratosphere, *Nat.*
1326 *Commun.*, 12(1), <https://doi.org/10.1038/s41467-021-26914-4>, 2021.
- 1327 López, J. A., Pineda, N., Montanyà, J., Velde, O. van der, Fabró, F., & Romero, D.: Spatio-
1328 temporal dimension of lightning flashes based on three-dimensional Lightning Mapping
1329 Array, *Atmos. Res.*, 197, 255–264, <https://doi.org/10.1016/j.atmosres.2017.06.030>,
1330 2017.
- 1331 Lorenz, R. D.: Lightning detection on Venus: A critical review. *Prog. Earth Planet. Sci.*, 5(1),
1332 <https://doi.org/10.1186/s40645-018-0181-x>, 2018.
- 1333 McCarthy, M. I., Rosmus, P., Werner, H.-J., Botschwina, P., & Vaida, V.: Dissociation of NH₃
1334 to NH₂+H, *J. Chem. Phys.*, 86(12), 6693–6700, <https://doi.org/10.1063/1.452417>,
1335 1987.
- 1336 Narita, T., Wanke, E., Sato, M., Sakanoi, T., Kumada, A., Kamogawa, M., Hirohiko, I., Harada,
1337 S., Kameda, T., Tsuchiya, F., & Kaneko, E.: A study of lightning location system (Blitz)
1338 based on VLF sferics, 2018 34th International Conference on Lightning Protection
1339 (ICLP), 1–7. <https://doi.org/10.1109/iclp.2018.8503311>, 2018.
- 1340 Oliva, F., D'Aversa, E., Migliorini, A., Piccioni, G., Poulet, F., Langevin, Y., Filacchione, G.,
1341 Ciarniello, M., Rodriguez, S., Seignovert, B., Mura, A., Fletcher, L.N., Zinzi, A.,
1342 Giardino, M., Lopinto, E., Sindoni, G., Plainaki, C.: JUICE-MAJIS Earth observations
1343 during the 2024 gravity assist: an overview and comparison with PRISMA data.
1344 Preprint egusphere-2025-6455 [submitted], <https://doi.org/10.5194/egusphere-2025-6455>, 2026.
- 1346 Orville, R. E.: High-speed, time-resolved spectrum of a lightning stroke, *Science*, 151(3709),
1347 451–452, <https://doi.org/10.1126/science.151.3709.451>, 1966.
- 1348 Orville, R. E.: Spectrum of the lightning stepped leader. *J. Geophys. Res.*, 73(22), 6999–7008,
1349 <https://doi.org/10.1029/jb073i022p06999>, 1968.
- 1350 Pérez-Invernón, F. J., Gordillo-Vázquez, F. J., Passas-Varo, M., Neubert, T., Chanrion, O.,
1351 Reglero, V., & Østgaard, N.: Multispectral optical diagnostics of lightning from space,
1352 *Remote Sens.*, 14(9), 2057, <https://doi.org/10.3390/rs14092057>, 2022.
- 1353 Petersen, W. A., Christian, H. J., & Rutledge, S. A.: TRMM observations of the global
1354 relationship between ice water content and lightning, *Geophys. Res. Lett.*, 32(14),
1355 <https://doi.org/10.1029/2005gl023236>, 2005.
- 1356 Peterson, M.: Making a Superbolt: Reconciling observations of the optically brightest lightning
1357 on Earth from different satellites, *Earth Space Sci.*, 10(8),
1358 <https://doi.org/10.1029/2023ea003001>, 2023.
- 1359 Peterson, M., & Rudlosky, S.: The time evolution of optical lightning flashes, *J. Geophys. Res.*
1360 *D: Atmospheres*, 124(1), 333–349, <https://doi.org/10.1029/2018jd028741>, 2019.
- 1361 Poulet, F., Langevin, Y., & Piccioni, G.: Calibration of the Moons And Jupiter Imaging
1362 Spectrometer (MAJIS): Introduction to the special collection and summary of the
1363 performances, *Rev. Sci. Instrum.*, 95(7), <https://doi.org/10.1063/5.0209679>, 2024a.
- 1364 Poulet, F., Piccioni, G., Langevin, Y., Dumesnil, C., Tommasi, L., Carlier, V., Filacchione, G.,

1365 Amoroso, M., Arondel, A., D'Aversa, E., Barbis, A., Bini, A., Bolsée, D., Bousquet, P.,
 1366 Caprini, C., Carter, J., Dubois, J.-P., Condamin, M., Couturier, S., Dassas, K., Dexet,
 1367 M., Fletcher, L., Grassi, D., Guerri, I., Haffoud, P., Larigauderie, C., Le Du, M.,
 1368 Mugnuolo, R., Pilato, G., Rossi, M., Stefani, S., Tosi, F., Vincendon, M., Zambelli, M.,
 1369 Arnold, G., Bibring, J.-P., Biondi, D., Boccaccini, A., Brunetto, R., Carapelle, A.,
 1370 Cisneros González, M., Hannou, C., Karatekin, O., Le Cle'ch, J.-C., Leyrat, C.,
 1371 Migliorini, A., Nathues, A., Rodriguez, S., Saggin, B., Sanchez-Lavega, A., Schmitt, B.,
 1372 Seignovert, B., Sordini, R., Stephan, K., Tobie, G., Zambon, F., Adriani, A., Altieri, F.,
 1373 Bockelée, D., Capaccioni, F., De Angelis, S., De Sanctis, M.-C., Drossart, P., Fouchet,
 1374 T., Gérard, J.-C., Grodent, D., Ignatiev, N., Irwin, P., Ligier, N., Manaud, N., Mangold,
 1375 N., Mura, A., Pilorget, C., Quirico, E., Renotte, E., Strazzulla, G., Turrini, D., Vandaele,
 1376 A.-C., Carli, C., Ciarnello, M., Guerlet, S., Lellouch, E., Mancarella, F., Morbidelli, A.,
 1377 Le Mouélic, S., Raponi, A., Sindoni, G. Snels, M.: : Moons and Jupiter Imaging
 1378 Spectrometer (MAJIS) on Jupiter Icy Moons Explorer (JUICE), *Sp. Sci. Rev.*, 220(3),
 1379 <https://doi.org/10.1007/s11214-024-01057-2>, 2024b.

1380 Poulet, F., Piccioni, G., Langevin, Y., Dumesnil, C., Carlier, V., Seignovert, B., Dexet, M., N.
 1381 Fletcher, L., Leyrat, C., Altieri, F., Carter, J., D'Aversa, E., De Sanctis, M., Grassi, D.,
 1382 Guerlet, S., Le Mouélic, S., Migliorini, A., Oliva, F., Royer, C., Rodriguez, S., Stephan,
 1383 K., Tosi, F., Zambon, F., Adriani, A., Arnold, G., Bibring, J.-P., Bockelée, D., Brunetto,
 1384 R., Capaccioni, F., Carli, C., Cavalié, T., Cisneros González, M., Ciarnello, M., De
 1385 Angelis, S., Drossart, P., Filacchione, G., Fouchet, T., Gérard, J.-C., Grodent, D., Irwin,
 1386 P., Jacquino, S., Karatekin, O., Lellouch, E., Ligier, N., Mangold, N., Mebsout, M.,
 1387 Merlin, F., Morbidelli, A., Mura, A., Nathues, A., E. Palumbo, M., Pilorget, C., Poch, O.,
 1388 Quirico, E., Raponi, A., Robert, S., Roussos, E., Sanchez-Lavega, A., Schmitt, B.,
 1389 Sindoni, G., Snels, M., Sordini, R., Stefani, S., Strazzulla, G., Trent, T., Tobie, G.,
 1390 Turrini, D., Vandaele, A.-C., Vincendon, M., Witasse, O., Vallat, C., and Moraino, A.:
 1391 ESA/JUICE encounters Earth/Moon in 2024: overview of the Moons And Jupiter
 1392 Imaging Spectrometer (MAJIS) observations, *Ann. Geophys.*, 44, 163–193.
 1393 <https://doi.org/10.5194/egusphere-2025-6191>, 2026.

1394 Prueitt, M. L.: The excitation temperature of lightning, *J. Geophys. Res.*, 68(3), 803–811,
 1395 <https://doi.org/10.1029/jz068i003p00803>, 1963.

1396 Rafi, M. H., & Mostafa, M. G.: Global lightning phenomena and time series model of lightning
 1397 flash radiance, 2022 International Conference on Energy and Power Engineering
 1398 (ICEPE), 1–6, <https://doi.org/10.1109/icepe56629.2022.10044878>, 2022.

1399 Rodriguez, S., Vincendon, M., Haffoud, P., Langevin, Y., Poulet, F., Quirico, E., Pilorget, C.,
 1400 Filacchione, G., Carter, J., Brunetto, R., Lecomte, B., Guiot, P., Dumesnil, C., &
 1401 Piccioni, G.: Calibration of MAJIS (Moons and Jupiter Imaging Spectrometer): V.
 1402 Validation with mineral samples and reference materials. *Rev. Sci. Instrum.*, 95(10),
 1403 <https://doi.org/10.1063/5.0215249>, 2024.

1404 Rudlosky, S. D., Goodman, S. J., Virts, K. S., & Bruning, E. C.: Initial geostationary lightning
 1405 mapper observations, *Geophys. Res. Lett.*, 46(2), 1097–1104,
 1406 <https://doi.org/10.1029/2018gl081052>, 2019.

1407 Ruscic, B.: Active thermochemical tables: Sequential bond dissociation enthalpies of methane,
 1408 ethane, and methanol and the related thermochemistry, *J. Phys. Chem. A*, 119(28),
 1409 7810–7837, <https://doi.org/10.1021/acs.jpca.5b01346>, 2015.

1410 Russell, C. T.: Planetary lightning, *Annu. Rev. Earth Planet. Sci.*, 21(1), 43–87,
 1411 <https://doi.org/10.1146/annurev.earth.21.050193.000355>, 1993.

1412 Salanave, L. E.: The optical spectrum of lightning, *Advances in Geophysics*, 10, 83–98,
 1413 [https://doi.org/10.1016/s0065-2687\(08\)60006-0](https://doi.org/10.1016/s0065-2687(08)60006-0), 1964.

1414 Salanave, L. E., Orville, R. E., & Richards, C. N.: Slitless spectra of lightning in the region from
 1415 3850 to 6900 Angstroms, *J. Geophys. Res.*, 67(5), 1877–1884,
 1416 <https://doi.org/10.1029/jz067i005p01877>, 1962.

1417 Schumann, U., & Huntrieser, H.: The global lightning-induced nitrogen oxides source, *Atmos.*
 1418 *Chem. Phys.*, 7(14), 3823–3907, <https://doi.org/10.5194/acp-7-3823-2007>, 2007.

1419 Simpson, J., Kummerow, C., Tao, W.-K., & Adler, R. F.: On the Tropical Rainfall Measuring

- 1420 Mission (TRMM). *Meteorol. Atmos. Phys.*, 60(1–3), 19–36,
 1421 <https://doi.org/10.1007/bf01029783>, 1996.
- 1422 Stefani, S., Piccioni, G., Poulet, F., Filacchione, G., Vincendon, M., Barbis, A., Tommasi, L.,
 1423 Guerri, I., Langevin, Y., Dumesnil, C., Haffoud, P., Rodriguez, S., Carter, J., Biondi, D.,
 1424 Boccaccini, A., De Angelis, S., Tosi, F., Pilorget, C., Guiot, P., & Lecomte, B.:
 1425 Calibration of MAJIS (Moons and Jupiter Imaging Spectrometer): VI. The inflight
 1426 calibration unit (ICU), *Rev. Sci. Instrum.*, 96(1), 011301,
 1427 <https://doi.org/10.1063/5.0221810>, 2025.
- 1428 Uman, M. A., & Orville, R. E.: Electron density measurement in lightning from stark-
 1429 broadening of H α . *J. Geophys. Res.*, 69(24), 5151–5154,
 1430 <https://doi.org/10.1029/jz069i024p05151>, 1964.
- 1431 Vincendon, M., Guiot, P., Lecomte, B., Condamin, M., Poulet, F., Arondel, A., Barbay, J.,
 1432 Carter, J., De Angelis, S., Dumesnil, C., Filacchione, G., Haffoud, P., Hansotte, J.,
 1433 Langevin, Y., Mayeur, P.-L., Piccioni, G., Pilorget, C., Quirico, E., & Rodriguez, S.:
 1434 Calibration of MAJIS (Moons And Jupiter Imaging Spectrometer). I. On-ground setup
 1435 description and characterization. *Rev. Sci. Instrum.*, 95(12), 121301,
 1436 <https://doi.org/10.1063/5.0226567>, 2024.
- 1437 Walker, T. D., & Christian, H. J.: Triggered lightning spectroscopy: 2. A quantitative analysis.
 1438 *J. Geophys. Res. D: Atmospheres*, 124(7), 3930–3942,
 1439 <https://doi.org/10.1029/2018jd029901>, 2019.
- 1440 Wang, P., Gong, S., Mo, Y.: Bond dissociation energy of O₂ measured by fully state-to-state
 1441 resolved threshold fragment yield spectra. *J. Chem. Phys.*, 160 (16), 164302,
 1442 10.1063/5.0207288, 2024.
- 1443 Warwick, J. W., Evans, D. R., Romig, J. H., Alexander, J. K., Desch, M. D., Kaiser, M. L.,
 1444 Aubier, M., Leblanc, Y., Lecacheux, A., & Pedersen, B. M.: Planetary radio astronomy
 1445 observations from Voyager 2 near Saturn, *Science*, 215(4532), 582–587,
 1446 <https://doi.org/10.1126/science.215.4532.582>, 1982.
- 1447 Wemhoner, J., Leal, A.F.R., da Silva, C.L. et al. Atomic oxygen photometric temperature of
 1448 lightning and its sub-processes with SOPAPILLA. *Sci Rep* 16, 4068,
 1449 <https://doi.org/10.1038/s41598-025-34189-8>, 2026.
- 1450 Wemhoner, J., da Silva, C. L., Leal, A. F. R., Bandara, S., Pantuso, J. G., & Sonnenfeld, R. G.
 1451 (2025). Near-infrared atomic oxygen photometry of lightning. *Journal of Geophysical*
 1452 *Research: Atmospheres*, 130, e2024JD042256.
 1453 <https://doi.org/10.1029/2024JD042256>, 2025.
- 1454 Wong, M. H., Kolmašová, I., Oyafuso, F. A., Imai, M., Mizumoto, S., Levin, S. M., et al: Radio
 1455 pulse power distribution of lightning in Jupiter's 2021–2022 stealth superstorms, *AGU*
 1456 *Advances*, 7, e2025AV002083. <https://doi.org/10.1029/2025AV002083>, 2026.
- 1457 Xu, L., Gou, X., Yuan, P., An, T., Jiang, R., & Deng, H.: Spectral study of rare upward
 1458 developing, circling, and branching cloud-to-ground lightning, *J. Geophys. Res. D:*
 1459 *Atmospheres*, 129(10), <https://doi.org/10.1029/2023jd040696>, 2024.
- 1460 Yingying A., Ping Y., Tingting A., Hong D., Shengxin H.: Hydrogen concentration in lightning
 1461 plasma channel and its effect on discharge characteristics. *J. Appl. Phys.* 138 (6),
 1462 063302. <https://doi.org/10.1063/5.0276142>, 2025.
- 1463 Zarka, P., & Pedersen, B. M.: Radio detection of uranian lightning by Voyager 2, *Nature*,
 1464 323(6089), 605–608, <https://doi.org/10.1038/323605a0>, 1986.
- 1465 Zhu, Y., Rakov, V. A., Tran, M. D., Stock, M. G., Heckman, S., Liu, C., Sloop, C. D., Jordan,
 1466 D. M., Uman, M. A., Caicedo, J. A., Kotovsky, D. A., Wilkes, R. A., Carvalho, F. L.,
 1467 Ngim, T., Gameraota, W. R., Pilkey, J. T., & Hare, B. M.: Evaluation of ENTLN
 1468 performance characteristics based on the ground truth natural and rocket-triggered
 1469 lightning data acquired in Florida, *J. Geophys. Res. D: Atmospheres*, 122(18), 9858–
 1470 9866, <https://doi.org/10.1002/2017jd027270>, 2017.